

EFFECTS OF SURFACE TENSION AND VISCOELASTIC BEHAVIOR ON THE THIN
FILM COATING FLOW OF MICROBICIDE GELS

By

Bin Hu

Submitted to the graduate degree program in Mechanical Engineering and the Graduate Faculty of
the University of Kansas in partial fulfillment of the requirements for the degree of Doctor of
Philosophy.

Chairperson Dr. Sarah L. Kieweg

Dr. Ronald L. Dougherty

Dr. Carl W. Luchies

Dr. Erik Van Vleck

Dr. Sara E. Wilson

Date defended: July 6th, 2016

The Dissertation Committee for Bin Hu certifies that this is the approved version of the following
dissertation:

EFFECTS OF SURFACE TENSION AND VISCOELASTIC BEHAVIOR ON THE THIN FILM
COATING FLOW OF MICROBICIDE GELS

Chairperson Dr. Sarah L Kieweg

Date approved:

ABSTRACT

Thin film coating flow is of importance in many fields, as well as for the design of polymeric drug delivery vehicles, such as anti-HIV topical microbicides. This dissertation describes a few models to investigate the coating flow of a microbicide gel.

At the beginning of this dissertation, we studied the gravity-driven thin film flow model. In our 2D (i.e. 1D spreading) power-law model, we found that surface tension effect not only impacted the spreading speed of the microbicide gel, but also had an influence on the shape of the 2D spreading profile. We observed a capillary ridge at the front of the fluid bolus. We focused on the capillary ridge in 2D flow and performed a series of simulations and showed how the capillary ridge height varies with other parameters. As shown in our results, we found that capillary ridge height increased with higher surface tension, steeper inclination angle, larger initial thickness, and more Newtonian fluids.

In the second study, a model of fingering instability at a moving contact line was developed. Previous literature showed that the emergence of a capillary ridge is strongly related to the contact line fingering instability in Newtonian fluids. Fingering instabilities during epithelial coating may change the microbicide gel distribution and therefore impact how well it can protect the epithelium. Results from our 2D model indicated more shear-thinning fluids should have suppressed finger growth and longer finger wavelength, and this should be evident in linear stability analysis (LSA) and 3D (i.e. 2D spreading) numerical simulations. In our 3D model

studies, we developed a LSA model for the gravity-driven flow of shear-thinning films, and carried out a parametric study to investigate the impact of shear-thinning on the growth rate of the emerging fingering pattern. A fully 3D model was also developed to compare and verify the LSA results using single perturbations, and to explore the result of multiple-mode, randomly imposed perturbations. Both the LSA and 3D numerical results confirmed that the contact line fingers grow faster for Newtonian fluids than the shear-thinning fluids on both vertical and inclined planes. In addition, both the LSA and 3D model indicated that the Newtonian fluids form fingers with shorter wavelengths than the shear-thinning fluids when the plane is inclined; no difference in the most unstable (i.e. emerging) wavelength was observed at vertical. For the first time for shear-thinning fluids, these results connect trends in capillary ridge and contact line finger formation in 2D models, LSA, and 3D simulations.

At the end of this dissertation, we used a more complicated constitutive model – the Phan-Thien-Tanner (PTT) rheological model -- to describe the viscoelastic behavior on two different models for the vehicle delivery process: the gravity-driven spreading model, and epithelial squeezing flow model. We used ANSYS POLYFLOW software package to solve the resulting PDEs. Elastic viscous split stress (EVSS) approach was used to split the stress tensor of the gel into a Newtonian solvent and an elastic polymeric contribution. Several parametric studies were carried out to investigate the combined effect of shear-thinning and elastic behavior on both flows. In the gravity-driven model, the spreading speed of the microbicide gel down an incline obtained from the current PTT model was slower than the one we found in the previous

power-law model. This is consistent with our previous numerical and experimental studies, which indicates the elastic effect of the microbicide gel is important and a more accurate constitutive model is needed than power-law model in simulating the microbicide spreading. In the epithelial squeezing flow model, we used the FSI (fluid-structure interaction) approach to study the spreading of the microbicide gel on the epithelial surface under the squeezing force of the vaginal tissue. The results showed that lower tissue elasticity and lower Deborah number of the microbicide gel can cause more epithelial deformation. Then microbicide gel flows faster with higher tissue elasticity during the insertion process.

The results of this dissertation can provide us insights on how to optimize non-Newtonian fluid properties for better performance during the drug delivery process.

ACKNOWLEDGEMENTS

I would like to thank my advisor, Dr. Sarah L. Kieweg for her great guidance and longtime support of my master and PhD studies. As an international student, whenever I have troubles, she is always willing to provide advice and help.

I also want to thank my committee for their time to evaluate my dissertation and defense.

My graduate studies were supported by NIH R21/R33AI082697 and NIH K12 HD052027. Some of the computational resources at the KU ITTC high performance computing cluster were funded by NSF MRI 0821625.

I would like to thank my lab group: Vitaly Kheyfets, Mark Pacey, Rajib. Anwar, Henry Clever and Thora Whitmore for all their help and teamwork.

I also extend my gratefulness to the KU-KUT Joint Master Program and KUT Professor Kwang Sun Kim's recommendation that provided opportunity to study in KU.

I thank my parents and my wife for their unconditional love and support.

TABLE OF CONTENTS

ABSTRACT.....	iii
ACKNOWLEDGEMENTS.....	vi
TABLE OF CONTENTS	vii
LIST OF FIGURES	x
NOMENCLATURE.....	xvii
1. INTRODUCTION	1
1.1. Background.....	1
1.2. Motivation	9
1.3. Guide to this dissertation	9
2. THE EFFECT OF SURFACE TENSION ON THE GRAVITY-DRIVEN 2D THIN FILM FLOW OF NEWTONIAN AND POWER-LAW FLUIDS	13
2.1. Introduction	13
2.2. Methods	16
2.2.1. Evolution equation.....	17
2.2.2. Numerical method	19
2.2.3. Model validation.....	20
2.3. Results and discussion	21
2.3.1. Capillary ridge	21

2.3.2. Parametric study	23
2.4. Conclusions	31
3. CONTACT LINE INSTABILITY OF GRAVITY-DRIVEN FLOW OF POWER-LAW FLUIDS.....	34
3.1. Introduction	34
3.2. Linear stability analysis	36
3.2.1. Methods of linear stability analysis	37
3.2.2. Results and discussion: LSA	42
3.3. 3D simulations	46
3.3.1. Finite element formulation	46
3.3.2. Numerical parameters.....	47
3.3.3. Results and discussion: 3D simulations.....	49
3.4. Conclusions	59
4. EFFECT OF VISCOELASTICITY ON SPREADING IN GRAVITY-DRIVEN AND SQUEEZING FLOWS.....	61
4.1. Introduction	61
4.2. PTT constitutive model	64
4.3. Gravity-driven spreading model.....	65
4.3.1. Problem description.....	65
4.3.2. Numerical methods.....	66

4.3.2.	Results and discussion	67
4.4.	Epithelial squeezing flow model	75
4.4.1.	Problem and methods	75
4.4.2.	Results and discussion	77
4.5.	Summary	82
5.	CONCLUSIONS AND FUTURE WORK	84
5.1.	General conclusions.....	84
5.2.	Limitations and future work	85
5.3.	Summary.....	89
6.	APPENDIX.....	90
	Appendix A: Sensitivity study of precursor thickness.....	90
	Appendix B: Similarity solution for power-law fluids	91
	Appendix C: Traveling wave solution for power-law fluids	93
	Appendix D: Non-dimensional study for 2D power-law fluids.....	94
	Appendix E. Fluorescence Imaging Measurement	97
7.	REFERENCES	101

LIST OF FIGURES

Figure 1-1. Illustration of a microbicide gel applied to the vaginal epithelium and covering the tissue due to tissue elasticity.	2
Figure 1-2. Surface tension forces acting on a tiny patch of surface.	5
Figure 2-1. Coordinate system diagram for 2D model of flow down an incline.	17
Figure 2-2. Evolution of free surface, total time=110 s, sampling=10 s. (Parameters used in the simulation: $m=100 \text{ Ps}^{n-1}$, $n=1$, $\alpha=60^\circ$, $\gamma=70 \text{ dyn/cm}$, $H=0.3 \text{ cm}$, $b=0.01 \text{ cm}$)	22
Figure 2-3. Comparison of free surfaces between the model without surface tension effect (black solid) and the surface tension model (red dashed) at $t=20 \text{ s}$. (Parameters used in the simulation: $m=100 \text{ Ps}^{n-1}$, $n=1$, $\alpha=60^\circ$, $\gamma=70 \text{ dyn/cm}$, $H=0.3 \text{ cm}$, $b=0.01 \text{ cm}$)....	22
Figure 2-4. Plot of the capillary ridge height h_{cr} (black solid and dotted lines, left axis) and spreading time (red dashed and dash-dot lines, right axis) as a function of surface tension coefficient γ for both Newtonian ($n=1$, solid and dashed lines) and shear-thinning fluids ($n=0.5$, dotted and dash-dot lines). (Parameters used in the simulation: $m=100 \text{ Ps}^{n-1}$, $\alpha=60^\circ$, $H=0.3 \text{ cm}$, $b=0.01 \text{ cm}$).....	25
Figure 2-5. Plot of the capillary ridge height h_{cr} (cm) as a function of n for different values of initial thickness H , with constant $m=400 \text{ Ps}^{n-1}$, $\alpha=60^\circ$, $\gamma=70 \text{ dyn/cm}$	27
Figure 2-6. Comparison of free surfaces between shear-thinning index $n=0.5$ (black solid) and $n=1$ (red dashed) when gel reaches $x=4 \text{ cm}$, with constant $m=400 \text{ Ps}^{n-1}$, $\alpha=60^\circ$,	

$\gamma=70$ dyn/cm and $H=0.3$ cm.....	28
Figure 2-7. (Color online) Comparison of free surfaces between initial thickness $H=0.2$ cm (black solid) and $H=0.45$ cm (red dashed) when gel reaches $x=4$ cm, with constant $m=400$ Ps^{n-1} , $n=0.7$, $\alpha=60^\circ$ and $\gamma=70$ dyn/cm.....	
	29
Figure 2-8. Plot of the capillary ridge height h_{cr} (cm) as a function of α for different values of initial thickness H , with constant $m=400$ Ps^{n-1} , $n=0.7$ and $\gamma=70$ dyn/cm. Note: a finer mesh between 10° and 40° for α was applied to handle the rapid change.....	
	30
Figure 2-9. Plot of the capillary ridge height h_{cr} (cm) as a function of α for different values of n , with constant $m=400$ Ps^{n-1} , $H=0.3$ cm and $\gamma=70$ dyn/cm. Note: a finer mesh between 10° and 40° for α was applied to handle the rapid change.....	
	31
Figure 3-1. The LSA growth rate as a function of wavenumber q and power-law index n . Comparison among different dimensionless numbers: $D=0$ (a), $D=0.5$ (b), $D=1$ (c) and $D=2$ (d). Figures (b), (d) and the vertical lines in Figures (a) and (b) will be discussed later in Section 3.3 in conjunction with 3D simulations. (Other simulation parameters: precursor $b=0.1$, $\Delta x=0.01$, $\Delta t=0.01$.).....	
	45
Figure 3-2. Effect of precursor thickness on LSA growth rate for a shear-thinning fluid: $b=0.01$ (black solid), $b=0.025$ (green dotted), $b=0.05$ (red circled), and $b=0.1$ (blue dotted). (Other simulation parameters: $n=0.8$, $D=0$, $\Delta x=0.01$, $\Delta t=0.01$)	
	45
Figure 3-3. Schematic of the boundary bonditions (BCs) for the 3D numerical simulation. The subscript on h indicates derivative. Flow is in the x -direction downhill to the	

right, and the domain width is Ly in the y -direction. The constant flux condition is the non-dimensional $h = 1$ at $x = 0$ for all time. The precursor boundary condition is indicated with $h = b \ll 1$ at the domain boundary $x = Lx$ for all time. 47

Figure 3-4. Time series of 3D simulations with single mode perturbation, for $D = 0$.

Growth of the fingering patterns for both Newtonian (Rows 1, 3, 5) and shear-thinning fluids (Rows 2, 4, 6) on a vertical plane ($D = 0$) with perturbations of different wavelengths $\lambda = 4\pi, 8.7$, and 2π . From left to right: $t = 0, 50$, and 100 . $Lx = 20$, $Ly = \lambda$ for each simulation. 50

Figure 3-5. Time series of 3D simulations with single mode perturbation, for $D = 1$.

Growth of the fingering patterns for both Newtonian (Rows 1, 3, 5) and shear-thinning fluids (Rows 2, 4, 6) on a less-inclined plane ($D = 1$) with perturbations of different wavelengths $\lambda = 8\pi, 18$, and 4π . From left to right: $t = 0, 100$, and 200 . $Lx = 20$, $Ly = \lambda$ for each simulation. 52

Figure 3-6. Comparison of growth rates from LSA (solid lines) and single mode 3D

simulations (symbols). The figure shows the finger length (normalized to initial length) vs. time for four cases: $n = 1, D = 0$; $n = 1, D = 1$; $n = 0.6, D = 0$; and $n = 0.6, D = 1$. For each case, the calculated growth from the 3D simulations (symbols) is compared to LSA prediction (solid lines). (All 3D simulations and LSA results used perturbations of wavelength $\lambda = 8\pi$ which provides a positive growth rate for all simulations.) 54

Figure 3-7. Time-series of 3D simulations with multiple-mode, random perturbations for $D = 0$. Comparison between (a) Newtonian $n = 1$ and (b) shear-thinning $n = 0.6$ on a vertical plane ($D = 0$, $Lx = 40$, $Ly = 96$). (Left to right, for $t = 0$, 60, and 120.)	56
---	----

Figure 3-8. A summary of contact line patterns for 12 simulation cases, each showing only one time point. The points selected were: $t = 60, 80, 100$ and 120 for $D = 0, 0.5, 1$ and 2 , respectively. These time points are in the regime when the LSA results correspond to the linear portion of the 3D numerical simulations in Figure 3-6. ($Lx = 40$, $Ly = 96$).	58
---	----

Figure 4-1. Illustration of a microbicide gel applied to the vaginal epithelium and covering of the tissue due to tissue elasticity.	64
--	----

Figure 4-2. Illustration of 2D viscoelastic flow down an incline. The side profile of the fluid is shown in dark blue. The white incline is a 60° inclination with respect to horizontal.	66
--	----

Table 4-1. Parameter settings for the first set of simulations, where λ is relaxation time, η_r is viscosity ratio, and ε is PTT model parameter, and total viscosity η and PTT parameter ξ are kept as constant, $\eta=200$ P and $\xi=0.01$.	68
---	----

Figure 4-3. Transient result of gravity-driven flow spreading length with varying parameters from Group (1) listed in Table 4-1.	69
--	----

Figure 4-4. Spreading length for different PTT parameters ε and ξ , with constant $\eta=200$ P,	
---	--

$\lambda=1$ s and $\eta_r=0.2$	70
Figure 4-5. Rheological data for a 2.0 % sodium carboxymethylcellulose gel. The dots indicate experimental rheological data, the solid lines show curve-fitting to the PTT constitutive equation, and the dotted line shows curve-fitting to the power-law constitutive equation.	72
Figure 4-6. Results of microbicide gel spreading for different models. The blue curve indicates the spreading speed from the PTT model simulation, while the red and black curves are the results from power-law models.....	74
Figure 4-7. Geometry and boundary condition of the model describing insertion of a microbicide gel (“fluid” in diagram) between the vaginal epithelial tissue.....	76
Figure 4-8. Contours of displacement in the tissue region (left contour map) and velocity in the fluid region (right contour map) for different tissue elasticities, with constant $E=5$ kPa (top) and $E=0.5$ kPa (bottom), with constant $Q=1$ cm ³ /sec, $\nu=0.25$, $\eta=200$ P, $\eta_r=0.2$, $\lambda=1$ s, $\varepsilon=0.01$, and $\xi=0.01$	79
Figure 4-9. Contours of displacement in the tissue region and velocity in the fluid region for two Poisson’s ratios, with constant $Q=1$ cm ³ /sec, $E=5$ kPa, $\eta=200$ P, $\eta_r=0.2$, $\lambda=1$ s, $\varepsilon=0.01$, and $\xi=0.01$	79
Figure 4-10. Contours of displacement in the tissue region and velocity in the fluid region for two inflow rates, with constant $E=5$ kPa, $\nu=0.25$, $\eta=200$ P, $\eta_r=0.2$, $\lambda=1$ s, $\varepsilon=0.01$, and $\xi=0.01$	80

Figure 4-11. Plot of displacement in the tissue region for different Deborah numbers and

constant $Q=1 \text{ cm}^3/\text{s}$, $E=5 \text{ kPa}$, $\nu=0.25$, $\eta=200 \text{ P}$, $\eta_r=0.2$, $\varepsilon=0.01$, and $\xi=0.01$ 81

Figure A.1. (Color online) Comparison of the free surfaces between the results for different

precursor thicknesses: $b=0.001 \text{ cm}$ (black solid), $b=0.01 \text{ cm}$ (blue dotted) and $b=0.05$

cm (red dashed). (Parameters used in the simulation: $m=100 \text{ Ps}^{n-1}$, $n=0.8$, $\alpha=60^\circ$, $\gamma=70$

dyn/cm , $H=0.3 \text{ cm}$) 90

Figure B.1. Comparison of the free surface spreading of the similarity solution (black solid)

and the numerical model at 110 s for Newtonian fluids. Two different initial conditions:

$H=0.2 \text{ cm}$ (red dashed) and $H=0.45 \text{ cm}$ (blue dotted). Parameters: $m=100 \text{ Ps}^{n-1}$, $n=1$,

$\alpha=60^\circ$ and $\gamma=0 \text{ dyn/cm}$ 92

Figure B.2. Comparison of the free surfaces spreading of the similarity solution (black solid)

and the numerical model at 110 s for shear-thinning fluids. Two different initial

conditions: $H=0.2 \text{ cm}$ (red dashed) and $H=0.45 \text{ cm}$ (blue dotted). Parameters: $m=100$

Ps^{n-1} , $n=0.5$, $\alpha=60^\circ$ and $\gamma=0 \text{ dyn/cm}$ 92

Figure C.1. Evolution of free surface using constant flux in the numerical simulation, total

time=10s, sampling=1s. (Parameters used in the simulation: $m=200 \text{ Ps}^{n-1}$, $n=0.9$, $\alpha=60^\circ$,

$\gamma=40 \text{ dyn/cm}$, $b=0.01 \text{ cm}$) 94

Figure D.1. Dimensionless maximum height of the flow profiles as a function of D for

different values of shear-thinning index n 97

Figure E.1. Example of the fingering patterns observed using the original ramp apparatus. 98

Figure E.2. Cross depth plot showing the evolution of free surface at the front of a finger, which can be used to compare the results in Chapters 2 and 3, e.g., Figure 2-2 and Figure C.1.	99
Figure E.3. 3D plot of a single propagating finger obtained and calculated using fluorescence imaging.	100

NOMENCLATURE

(Note: The variables with no units indicate that they are dimensionless quantities. In Chapter 3, all the parameters are kept dimensionless, since the whole chapter is a non-dimensional study.)

p	Pressure, dyn/cm ²
h	Height or thickness of the thin film fluid, cm
γ	Surface tension coefficient, dyn/cm
k	Curvature of a surface area
τ	Stress tensor for fluids, dyn/cm ²
τ_s	Newtonian solvent contribution of the stress tensor, dyn/cm ²
τ_p	Polymeric contribution of the stress tensor, dyn/cm ²
$\overset{\nabla}{\hat{\tau}}_p$	Lower convected time derivatives of τ_p , dyn/cm ²
$\overset{\Delta}{\hat{\tau}}_p$	Upper convected time derivatives of τ_p , dyn/cm ²
m	Consistency of power-law fluid, Ps ⁿ⁻¹
n	Power-law index or shear-thinning index
D	Shear rate tensor, s ⁻¹
$\dot{\gamma}$	Characteristic shear rate
\tilde{v}	Velocity vector, cm/s
u	Velocity in the x direction, cm/s

v	Velocity in the y direction, cm/s
η	Total viscosity, Poise or P
η_s	Newtonian contribution viscosity, P
η_p	Polymeric contribution viscosity, P
η_r	Viscosity ratio, η_s / η
λ	Relaxation time, s
ξ	PTT parameter
ε	PTT parameter
α	Inclination angle, rad
ρ	Density, g/cm ³
g	Standard gravity, 98.0665 cm/s ²
b	Thickness of the precursor, cm
H	Characteristic height, cm
U	Characteristic velocity, cm/s
D	Dimensionless parameter representing the magnitude of the normal component of gravity force
C_a	Capillary number
σ	Growth rate of the perturbation

q	Wavenumber of the perturbation
λ	Wavelength of the perturbation
G'	Storage modulus, dyn/cm ²
G''	Loss modulus, dyn/cm ²
E	Young's modulus, dyn/cm ²
ν	Poisson's ratio
σ	Stress tensor for solids, dyn/cm ²
ε	Strain tensor
D_e	Deborah number
Q	Volumetric flow rate, cm ³ /s

1. INTRODUCTION

1.1. Background

HIV and microbicides

The human immunodeficiency virus (HIV) / acquired immunodeficiency syndrome (AIDS) pandemic is the world's greatest public health crisis. According to the UNAIDS Global Update [1], with about 2.1 million people newly infected in 2015, there are now an estimated 36.7 million people around the world who are living with HIV in 2015.

Although the overall growth of the global HIV/AIDS pandemic appears to have stabilized in the past decade, levels of new infections overall are still high [1]. Especially for women, HIV/AIDS is still the leading cause of death and disease among women between the ages of 15 and 44 [2].

Many studies have shown that microbicides can be a promising solution for the prevention of HIV transmission during sexual intercourse [3-5]. Microbicides usually consist of an anti-HIV active agent in some delivery vehicle, such as a gel, cream or foam. They are delivered to vaginal and/or rectal epithelia to protect them from HIV and other sexually transmitted infections (STI) [6]. Microbicides may provide a physical barrier [7], amplify the normal vaginal defense, destroy the pathogens chemically, or inhibit viral infection [8]. Microbicides are a preventive intervention to provide a low-cost, controlled by women method for protection against HIV. A microbicide will protect women who do not have access to condoms or the ability to negotiate

condom protection for socioeconomic reasons. Condoms are not used consistently and correctly, and unprotected sex remains widespread [4]. AIDS vaccines may ultimately solve the HIV pandemic. However, AIDS vaccines are proving to be a technical challenge and may not be achieved in the immediate future. There is, therefore, an urgent need for a microbicide to prevent new HIV infections [3-5].

Microbicide delivery

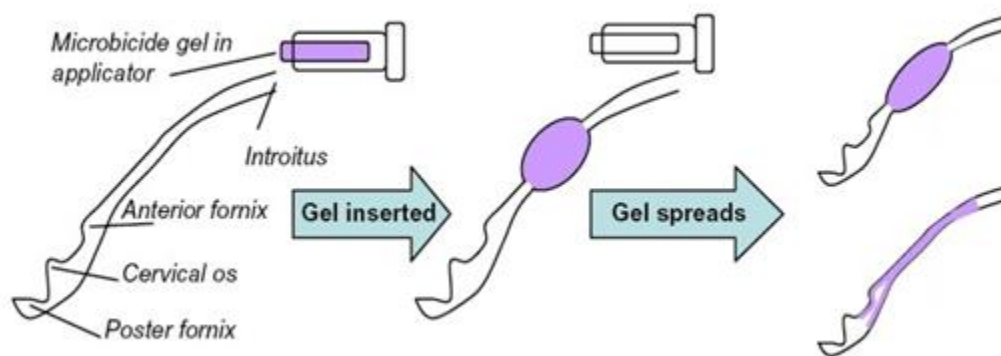


Figure 1-1. Illustration of a microbicide gel applied to the vaginal epithelium and covering the tissue due to tissue elasticity.

There are a few options for applying microbicide gels to the vaginal epithelium. The method shown in Figure 1-1 (a) (b) is to use an applicator. After application and removal of the applicator, the microbicide gel will be squeezed by the deformed epithelial surface and spread further to the anterior and poster fornixes, as shown in Figure 1-1 (c). To prevent HIV, we need the microbicide to coat the entire vaginal epithelium. Recent study has shown that the current gap in microbicide development is the delivery vehicle design [9]. It is challenging to design a drug delivery vehicle to coat the epithelial surface completely without leaving any ‘dry’ spots,

and remain on the surface while under external forces, such as gravity and squeezing.

Engineering approach

This dissertation is one of the components of a larger research project on examining how to optimize microbicides. The long-term goal of the overall project is to design delivery vehicles (e.g., polymer solutions or “gels”) with optimized physicochemical properties and desired microbicidal activity. To achieve this goal, our research group is working on the following subprojects: (1) determining the relationship between the vehicle physicochemical properties and the vehicle spreading performance/function, (2) measuring squeezing forces and the elastic modulus of human vaginal tissue *in vivo*, (3) quantifying relationships between molecular structure and physicochemical properties of delivery vehicles and (4) ultimately obtaining the molecular structure-property-function relationship for optimal design of the microbicides.

This dissertation is a part of element (1). It is to determine the relationship between the physicochemical properties, e.g., rheological properties, and the vehicle spreading performance, e.g., contact line patterns, and the vehicle-epithelium interaction.

As a step towards this goal, in this dissertation, we develop mathematical tools to describe the vehicle performance in response to several forces when microbicide gels are delivered to the vagina. These forces can include gravity, squeezing, shearing and surface tension. We separate them into two different models, the gravity-driven flow model and the squeezing flow model, to isolate the impacts of gravity and squeezing force and to simplify the problem. Shear stress is

incorporated into both flow models. Surface tension is only examined in the gravity-driven flow model.

Gravity-driven thin film flow

There are many industrial applications in which gravity-driven thin film flow is of interest. Among these are paints [10], contact lens manufacture [11] and microchip fabrication [12]. Gravity-driven thin film flow also occurs throughout nature, including a variety of gravity currents, such as lava flow and glacier flow [13, 14]. For the application of drug delivery vehicles, gravity can also influence the gel flow greatly along the epithelial surface due to the orientation of the vaginal axis and/or changes in posture.

There are a few approaches when solving the thin film spreading problem. The lubrication approximation is the most commonly used approach [15, 16]. It can simplify the Navier-Stokes equations by assuming the thickness of the fluid is very small compared to the length of the flow domain. Most of our computational studies for gravity-driven flow are within the scope of lubrication theory. In the previous work of our research group on gravity-driven spreading, we developed experimental and numerical models (2D and 3D) of a finite bolus flowing down an incline [4, 17, 18].

Surface tension effect

There is a tension effect in the liquid surface because of uneven molecular force of attraction

at or near the surface. Since discontinuous changes of fluid properties can cause rapid changes in molecular forces, surface tension is an inherent property between material interfaces [19].

If no force acts normal to a tensioned surface, the surface must remain flat. But if the pressure on one side of the surface differs from pressure on the other side, that pressure difference multiplied by the surface area results in a normal force. In order for the surface tension forces to cancel the force due to pressure, the surface must be curved. When all the forces are balanced (see Figure 1-2), the resulting equation is known as the Young–Laplace equation [20]:

$$\Delta p = \gamma \left(\frac{1}{R_x} + \frac{1}{R_y} \right) \quad (1)$$

where:

Δp is the pressure difference.

γ is surface tension coefficient (dyn/cm).

R_x and R_y are radii of curvature in each of the axes that are parallel to the surface.

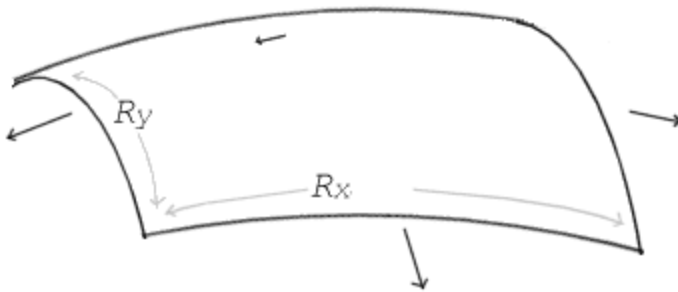


Figure 1-2. Surface tension forces acting on a tiny patch of surface.

There is a small curvature approximation used for thin film flow [21]:

$$k = \nabla^2 h = \frac{\partial^2 h}{\partial x^2} \quad (2)$$

Using the lubrication approach, we can incorporate the surface tension effect as a boundary condition for the pressure term of the thin film equation, as done in many studies (e.g., Refs.[16, 22-24]).

Squeezing flow

Squeezing forces generated by vaginal tissue also have a great impact on the epithelial flow. One of our group's previous studies examined the thin film flow of power-law fluids under the influence of tissue elasticity after the insertion of the gel, as shown in Figure 1.1 (b) and (c). In that study, the initial shape of the gel was assumed to be a parabola, and tissue elasticity was incorporated in the pressure term of the momentum equation. Chapter 4 of this dissertation will focus on the interaction between the elasticity of the tissue and the flow of the gel during the insertion process, as shown in Figure 1-1 (a) and (b). The objective is to investigate the interaction between tissue and gel, and to understand how important both the tissue elasticity and the elastic effect of the gel are on the tissue deformation and the velocity profile of the flow. Moreover, this study is a good supplement for our previous elastic boundary spreading study [25]. The results of this study can be a more practical initial condition for the later spreading process.

In order to correctly model tissue deformation, we need to couple the previously developed flow model with a deformable soft tissue model. Fluid-structure interaction (FSI) models are a

common approach for these types of flows. To our knowledge, there are no existing FSI studies for vaginal epithelial coating flows. However, there are many FSI studies for blood flow, for example Refs. [26-28]. Those studies are focused on the effect of the flow on wall stress for certain tissues in the cardiovascular system, e.g., arteries and heart valves. Due to the complication of the problem and difficulties in solving for the moving interface, most of those studies used commercial CFD package, Fluent, and assumed that the fluid was Newtonian. In this study, we will use POLYFLOW and its built-in FSI model.

Non-Newtonian rheology

Microbicides are polymeric liquids or gels that exhibit non-Newtonian behavior. In mathematical models, to connect these vehicle properties to performance, we use non-Newtonian fluid mechanics to describe gel flow.

Several constitutive models are considered in this dissertation. First we start with the power-law constitutive model [29]:

$$\tau_{ij} = m |II_{2D}|^{\frac{n-1}{2}} (2D_{ij}) \quad (3)$$

where $\tilde{\tau}$ is the stress tensor, m is the consistency of the power-law fluid, n is the power-law index or shear-thinning index, $2\tilde{D} = (\nabla \tilde{v})^T + \nabla \tilde{v}$ is the shear rate tensor, \tilde{v} is the velocity vector, and $II_{2D} = (1/2) \left[\left(\text{tr} 2\tilde{D} \right)^2 - \text{tr} \left(2\tilde{D} \right)^2 \right]$ is the second invariant of the shear rate tensor.

A 2D (i.e., 1D spreading in the axial direction) version can be simplified to

$$\tau_{zx} = m \left| \partial u / \partial z \right|^{n-1} \partial u / \partial z \quad (4)$$

where u is velocity in the axial direction.

The power-law model is a simple non-Newtonian constitutive model and can describe the shear-thinning behavior of microbicide gels. However, it is not very accurate at low shear-rates [30].

I use the power-law model as the constitutive model for the majority of this dissertation.

From our research group, Kheyfets also studied the Ellis model to address the limitations of the power-law model in the low shear-rate region [31]. The Ellis constitutive equation is:

$$\frac{1}{\eta} = \frac{1}{\eta_0} \left(1 + \left[\frac{\tau}{\tau_{1/2}} \right]^{\frac{1}{n}-1} \right) \quad (5)$$

where η_0 is the zero shear rate viscosity, and $\tau_{1/2}$ is the stress at which the apparent viscosity has dropped to half of its zero-shear viscosity value.

In addition to shear-thinning, microbicide gels also exhibit viscoelastic behavior. Various viscoelastic constitutive models have been published. Favero et al. tested several commonly used constitutive models and their performance for contraction flow [32]. Among those models, Phan-Thien-Tanner (PTT) is considered one of the most realistic models [33].

The constitutive equation for the PTT model [29] is

$$\boldsymbol{\tau} = \boldsymbol{\tau}_s + \boldsymbol{\tau}_p \quad (6)$$

The elastic viscous split stress (EVSS) approach is used to split the stress tensor of the gel, $\boldsymbol{\tau}$, into a Newtonian solvent contribution, $\boldsymbol{\tau}_s$, and an elastic polymeric contribution, $\boldsymbol{\tau}_p$.

The constitutive equation is a combination of the two contributions:

$$\boldsymbol{\tau}_s = 2\eta_s \mathbf{D}$$

$$\exp\left[\frac{\epsilon\lambda}{\eta_p}(\tau_p)\right]\tau_p + \lambda\left[\left(1 - \frac{\xi}{2}\right)\hat{\tau}_p^{\nabla} + \frac{\xi}{2}\hat{\tau}_p^{\Delta}\right] = 2\eta_p \mathbf{D} \quad (7)$$

where λ is the relaxation time, $\hat{\tau}_p^{\nabla}$ and $\hat{\tau}_p^{\Delta}$ are the lower and upper convected time derivatives of τ_p , ξ and ϵ are the PTT parameters, \mathbf{D} is the rate of deformation tensor, and η_s and η_p are the Newtonian solvent viscosity and polymeric viscosity. The viscosity ratio η_r can be defined as η_s / η , where total viscosity, η is $\eta_s + \eta_p$.

1.2. Motivation

In my master thesis, I carried out numerical simulations to study the effect of surface tension on the gravity-driven thin film flow of Newtonian and power-law fluids down an incline. The major finding in that study was that a capillary ridge at the front of the fluid bolus is caused by the incorporation of surface tension into the 2D power-law model [34]. Previous literature shows that the emergence of a capillary ridge is strongly related to the contact line fingering instability for Newtonian fluids, e.g., Ref. [16]. Fingering instabilities during epithelial coating may change the microbicide gel distribution and therefore impact how well it can protect the epithelium. After the completion of my master study, I was still interested in the follow-up problems, such as the relationship between capillary ridge and the fingering instability, and the effect of non-Newtonian rheology on fingering instability. These interesting topics motivated the start of my PhD study.

1.3. Guide to this dissertation

In this section, I want to outline the structure of this dissertation and explain some connections and logic among these relatively independent chapters.

As the first step of my PhD work, I expanded the initial study from my master thesis with additional validations and more systematic analysis [35]. This extensional work was also considered the first objective of my PhD study:

Chapter 2: The effect of surface tension on the gravity-driven 2D thin film flow of Newtonian and power-law fluids.

In this Chapter, I developed a 2D power-law model with incorporation of surface tension for gravity-driven thin film flows and examined how important surface tension is in such flows.

This work is an expansion of my master thesis, and the differences are summarized here. To assess of the numerical code, several validations including a convergence test, a mass conservation check, a similarity solution, a traveling wave solution, and a non-dimensional study, were added to compare with the existing results for Newtonian fluids in the literature. A more organized parametric study was carried out to investigate the influence of various parameters on the capillary ridge, caused by the surface tension effect.

The results of this study (in Chapter 2) leads to some follow-up questions:

- (1) What's the connection between the capillary ridge and contact line instability? We modeled 2D flow in Chapter 2, but how should we model 3D flow and fingering instabilities? This is addressed in the study described in Chapter 3.
- (2) The power-law model can only describe the shear-thinning behavior of the gel. But like

other polymeric liquid solutions, microbicide formulations exhibit both viscous and elastic behavior. Is there a better constitutive model to describe the combined shear-thinning and viscoelastic behavior? And can it be incorporated into the flow models? This is addressed in Chapter 4.

- (3) Gravity-driven flow down an incline is assumed to simplify the mathematical modeling in the above-mentioned problems. But unlike the solid wall of an inclined surface, elasticity of the tissue may have a big influence on the epithelial spreading. Is it possible to develop a model to describe the interaction between the gel flow and the tissue deformation? This is addressed in Chapter 4.

Chapter 3: Contact line instability of gravity-driven flow of power-law fluids.

Chapter 3 presents a contact line model using linear stability analysis to study the relationship between the capillary ridge and fingering instabilities, and how the shear-thinning effect influences the fingering instabilities. This chapter also expanded the current 2D model into 3D to simulate the fingering instabilities; and parametric studies were performed to investigate how contact line instability is affected by various fluid properties.

Chapter 4: Numerical analysis of gravity-driven spreading and epithelial squeezing flow of microbicide drug delivery using PTT constitutive model.

The objective of Chapter 4 was to incorporate a better constitutive model into our gravity-driven thin film flow and epithelial squeezing flow models, in order to study the impact of the viscoelastic behavior of the fluids on both flows.

2. THE EFFECT OF SURFACE TENSION ON THE GRAVITY-DRIVEN 2D THIN FILM FLOW OF NEWTONIAN AND POWER-LAW FLUIDS

The study described in this chapter has been published as Ref. [35]:

Hu, B. and S.L. Kieweg, *The effect of surface tension on the gravity-driven thin film flow of Newtonian and power-law fluids*. Computers & Fluids, 2012. 64: p. 83-90.

2.1. Introduction

As mentioned in the introductory chapter, the optimal design of microbicides during epithelial spreading is the reason we want to study gravity-driven thin film flow. But this study is not limited in the application of drug delivery vehicles. There are many industrial applications in which gravity-driven thin film flow is of interest. Among these are paints [10], contact lens manufacture [11] and microchip fabrication [12]. Gravity-driven thin film flows also occur throughout nature, including a variety of gravity currents, such as lava flow and glacier flow [13, 14]. All of these flows can be modeled using very similar methods. However, since the study of these flows focuses on tracing the change of the free surface, a question must be raised here: is surface tension important? This chapter is intended to develop a mathematical tool for understanding how important a role the surface tension plays in such flows.

In the previous work of our research group on gravity-driven spreading, we developed experimental and numerical models (2D and 3D) of a finite bolus of non-Newtonian fluid

(power-law or Herschel-Bulkley) flowing down an incline [4, 17, 18]. The study in this chapter considers the effect of surface tension of the liquid in the 2D power-law model.

To simulate surface tension, many studies have used the volume of fluids (VOF) Method coupled with the continuum surface force (CSF) method [36-40], which was originally developed by Brackbill et al. [19]. Basically, they treat surface tension as a volumetric force acting on a fluid near an interface and incorporate the surface tension effect as a source term in the Navier-Stokes equations. Therefore, VOF+CSF can be used to solve full Navier-Stokes equations for general fluid dynamics problems. However, for the thin film flow problems we are studying, we can reduce the Navier-Stokes equations to a single thin film equation using the well-known lubrication approximation. Through this approach, we used the Young–Laplace equation, which states that surface tension results in a net normal force directed toward the center of curvature of the interface. Thus, we can incorporate the surface tension effect as a boundary condition for the pressure, as done in many studies (e.g., [16, 22-24]). Although the computational scheme and post-analysis can both benefit from the simplified model, the limitation for this method is that it is hard to simulate the influence of contact angle. However, contact angles vanish when assuming complete wetting, as done in this study.

Previous literature using linear stability analysis (LSA) has shown that the “capillary ridge” occurring in the lengthwise direction was strongly related to the contact line “fingering instability” in the transverse direction [15, 16, 24, 41-43]. The term capillary ridge describes the bump showing at the front of the spreading fluid, while fingering instability describes how the

moving contact line at the front corrugates during flow. Schwartz [44] studied contact line instability numerically and for the first time showed that surface tension effects controlled the instability. Troian et al. [43] initially developed LSA on thin film flow and illustrated that the “bump” was responsible for the linear instability. Bertozzi and Brenner [16] showed that the transient growth of contact line instability explained why the critical inclination angle observed in LSA did not match experiments. They also verified that when a capillary ridge in the profile disappeared, the front contact line was linearly stable. Kondic and his research group [15, 16, 24, 41, 45, 46] also numerically studied 3D flow to simulate fingering instability in the transverse direction. These studies provided insights for our 3D flow study. Recently, Lin and Kondic [47] studied the instability of a thin film flowing down an inverted incline. Because hanging flow also occurs in microbicide epithelial coating processes, it is also one of our future research interests.

All of the above mentioned studies were done using a constant flux assumption, which means that the thickness of fluid behind and in front of the contact line is constant [15, 24, 41, 42, 45, 47, 48]. The constant flux assumption is not appropriate in our case, because the epithelial spreading flow case is “constant volume,” rather than “constant flux”, and the fluid layer thins over time. There are some limitations and complications to apply LSA on constant volume flow. Gonzalez et al. [49] developed a predictive model for the constant volume case by applying LSA results of the constant flux case. Gomba et al. [50] developed an integral method to study the linear stability of constant volume flow.

The above-mentioned studies inspired the idea of using the capillary ridge as an indicator for fingering instability and motivated this study, because when we add the surface tension effect to our 2D numerical simulation of a power-law fluid, in some cases we observe a capillary ridge in the 2D profile at the front of the fluid bolus. We also found that most of the studies mentioned above have assumed Newtonian fluids [15, 16, 24, 41-47, 49, 50], except Balmforth et al. [48] studied the instability of Bingham fluids using LSA and showed the effect of yield stress stabilized the contact line. To the authors' knowledge, the connection between surface tension effect and shear-thinning rheological properties for non-Newtonian fluids has not appeared in the literature. But the capillary ridge and fingering instability can also be observed in our experimental studies for shear-thinning fluids.

The goal of this study is to incorporate surface tension in the numerical 2D power-law model and use it for a parametric analysis. The main research questions are: (1) Under what flow parametric conditions does surface tension have an influence on shape or spreading? (2) When and under what kind of circumstances does the capillary ridge occur and increase?

2.2. Methods

2.2.1. Evolution equation

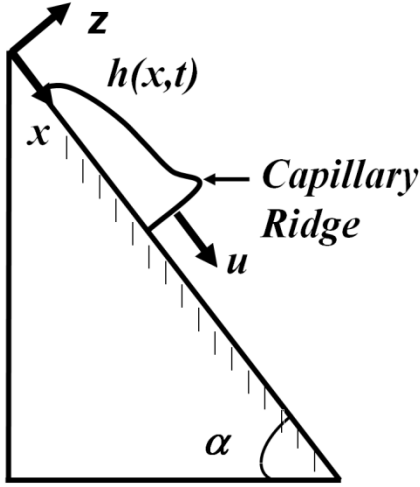


Figure 2-1. Coordinate system diagram for 2D model of flow down an incline.

In this section, we develop an evolution equation to apply numerical methods for flow calculations. The equation uses the height of the fluid as a function of spatial location and time ($h(x, t)$) to describe the movement of the fluid's free surface. Figure 2-1 illustrates the coordinate system for flow down an incline with inclination angle α . Only x and z directions are considered in this 2D model.

We follow the theoretical approach from our previous work [4, 34], and combine conservation of momentum and mass, the no-slip boundary condition, thin film lubrication approximations [51], and the power-law constitutive equation, $\tau_{zx} = m |\partial u / \partial z|^{n-1} \partial u / \partial z$, where τ is shear stress tensor, u is velocity in the axial direction, m is consistency, and n is the shear-thinning index.

To incorporate the surface tension effect, we use the Young–Laplace equation [19] $\Delta p = \gamma k$ to get pressure equilibrium at the free surface, where Δp is the pressure difference at the fluid-air interface, γ is surface tension coefficient, and k is curvature of the interface. The free surface in this study is a 1D curve. The curvature for a 1D curve is $k = |h''(x)| / (1 + h'(x)^2)^{3/2}$, which is positive and indicates $\Delta p > 0$ in the Young–Laplace equation. Because surface tension results in a net normal force directed toward the center of curvature of the interface [19], the pressure formulation at the gel-air interface is,

$$p_{gel} = p_{air} - \gamma \frac{h''(x)}{(1 + h'(x)^2)^{3/2}}. \quad (1)$$

This holds for both the convex curve ($h''(x) < 0$) and the concave curve ($h''(x) > 0$).

A small slope is assumed according to the thin film approximation, and Eq. (1) reduces to

$$p_{gel} = p_{air} - \gamma h''(x). \quad (2)$$

We used this pressure formulation (Eq. (2)) for the pressure term in the conservation of momentum equation, and we derived our governing evolution equation. Refer to [34, 52, 53] for more details about the derivation.

$$\frac{\partial h}{\partial t} + m^{-\frac{1}{n}} \frac{n}{2n+1} \frac{\partial}{\partial x} \left\{ h^{\frac{1}{n}+2} \left[\rho g (\sin \alpha - \cos \alpha \frac{\partial h}{\partial x}) + \gamma \frac{\partial^3 h}{\partial x^3} \right]^{\frac{1}{n}-1} \left[\rho g (\sin \alpha - \cos \alpha \frac{\partial h}{\partial x}) + \gamma \frac{\partial^3 h}{\partial x^3} \right] \right\} = 0.$$

(3)

All of the parameters in Eq. (3) were kept in dimensional form for the rest of this study because we want this study to provide insight into our future experimental work. Thus, showing isolated parameters and the critical values of these parameters in dimensional form is very important to this analysis. In Appendix D, which also utilizes Appendices A-C, a non-dimensional study of Eq. (3) is carried out and compared to existing Newtonian results in the literature.

2.2.2. Numerical method

The numerical method used to solve this nonlinear PDE (3) was an implicit finite difference scheme. We applied backward difference for the time derivative and central difference for the space derivatives. We then used Newton's method to solve the full set of nonlinear algebraic equations resulting from finite difference discretization. Each iteration of Newton's method then involved a large set of linear equations, which was solved by the LU decomposition method. These processes were coded using C++.

The computational domain for the simulations in this study was 10 cm long [0, 10 cm] in the x -direction. We used a parabolic initial condition profile to start the flow. The free surface for this parabolic initial condition can be described as a function,

$$h(x) = \begin{cases} H(1 - (x-2)^2), & 1 \leq x \leq 3 \\ b, & \text{other domain} \end{cases},$$

where H is the initial center height of the parabola, and b is the thickness of the thin film preceding the front, called the precursor. We added a precursor because there is a surface tension singularity caused by the 4th-order derivatives in Eq. (3). Refer to [54] for details. We used $b=0.01\text{cm}$ for all simulations in this study. Appendix A shows the sensitivity study of the precursor thickness b . The tolerances for the LU decomposition method and Newton's method were both set to $1\text{e-}4$. The time step, Δt , was set to 0.001 s , and the spatial mesh interval was 0.002 cm .

2.2.3. Model validation

We validated our new model in the following four ways:

- 1) We performed a convergence test. The free surface height $h(x, t)$ converges for both space and time mesh refinement.
- 2) We monitored the total volume of the gel as a function of time, and the results showed it holds for conservation of mass.
- 3) The results of the new surface tension model for $\gamma=0$ agreed with the similarity solution for power-law fluids, as well as the results of the previous model for a power-law fluid without consideration of surface tension [4]. Comparison between the numerical model results and the similarity solution is discussed in Appendix B.

- 4) By assuming a simplified constant flux flow, we compared the result from our numerical model to the traveling wave solution. We found that they agreed well with each other.

Please refer to Appendix C for details.

2.3. Results and discussion

In Sec. 2.3.1, we highlight the surface tension effect and appearance of the capillary ridge. In Sec. 2.3.2, first, we isolated the effect of surface tension on capillary ridge height and the spreading speed for both Newtonian and shear-thinning fluids. We also selected a surface tension coefficient value for the other parametric studies. Then, we explored how the other terms in the evolution equation (Eq. (3)) interact with each other and impact the capillary ridge height. The relevant parameters in the evolution equation (Eq. (3)) are:

m : consistency of the gel,

n : shear-thinning index of the gel,

α : inclination angle,

H : initial thickness, and

γ : surface tension coefficient.

2.3.1. Capillary ridge

As mentioned in introduction, surface tension dominates at the front of the flow and therefore causes the capillary ridge. We also witnessed this phenomenon in our simulations when we added the surface tension effect.

The following simulations use a Newtonian fluid with initial thickness $H=0.3$ cm, consistency $m=100 \text{ Ps}^{n-1}$, shear-thinning index $n=1$, inclination angle $\alpha=60^\circ$ and surface tension coefficient $\gamma=70 \text{ dyn/cm}$, as an example. A variety of parametric studies for non-Newtonian fluids are covered in the parametric study section.

Figure 2-2 shows the free surface plot from the new surface tension model during a 110 s period with 10 s time sampling. A very similar side profile is also obtained in Gomba et al.'s constant volume study for Newtonian fluids [50]. We compare our new surface tension model with our previous model [4] in Figure 2-3.

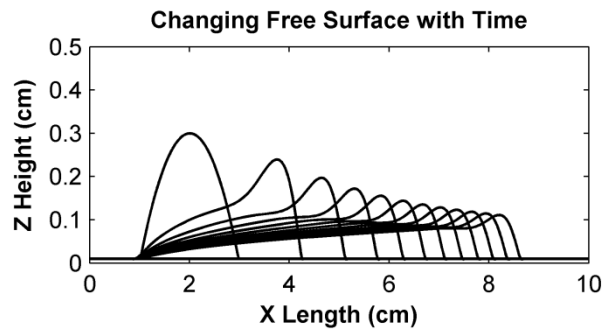


Figure 2-2. Evolution of free surface, total time=110 s, sampling=10 s. (Parameters used in the simulation: $m=100 \text{ Ps}^{n-1}$, $n=1$, $\alpha=60^\circ$, $\gamma=70 \text{ dyn/cm}$, $H=0.3 \text{ cm}$, $b=0.01 \text{ cm}$)

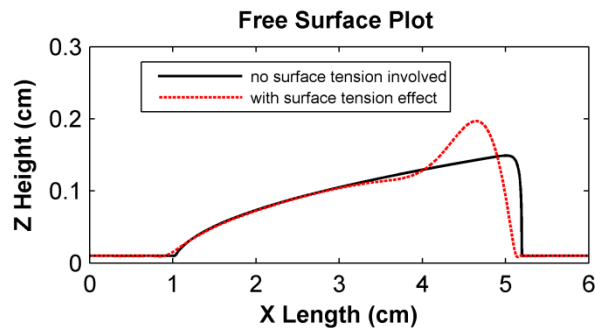


Figure 2-3. Comparison of free surfaces between the model without surface tension effect (black

solid) and the surface tension model (red dashed) at $t=20$ s. (Parameters used in the simulation: $m=100 \text{ Ps}^{n-1}$, $n=1$, $\alpha=60^\circ$, $\gamma=70 \text{ dyn/cm}$, $H=0.3 \text{ cm}$, $b=0.01 \text{ cm}$)

We can see that the capillary ridge occurs in the new model after incorporating the surface tension effect. In Figure 2-3, the red dashed plot shows a capillary ridge at the front of the flow. Moreover, the surface tension effect influences the spreading speed by holding the fluid and making it flow slower.

2.3.2. Parametric study

In this section, a series of simulations were carried out to investigate how the parameters influence the capillary ridge size. Here, we first focused on our main subject – surface tension. Then, we examined how the other terms in the evolution equation interact with each other and influence the capillary ridge.

We defined the capillary ridge height function as $h_{cr} = h_{\max} - h_{\max}|_{\gamma=0}$, where h_{\max} is the maximum height of the free surface for a given case, and $h_{\max}|_{\gamma=0}$ is the maximum height of the free surface under the assumption that all other parameters in the simulation are the same, and only surface tension effect is not incorporated. Note that this calculation of h_{cr} is only an approximation of the capillary ridge height due to the flow behavior difference between the non-zero surface tension case and zero surface tension case. An alternate definition can be

defined using a true capillary ridge height, but we did not select that method because it requires an arbitrary selection of the beginning of the ridge.

Due to different values of parameters, the spreading shape and speed of the simulations were very different. So for a better comparison, we didn't choose a certain instance in time to compare the differences among these cases. Instead, we calculated the capillary ridge height for each case when the flowing front reached the same position: $x=4$ cm.

Because surface tension is the actual cause of the capillary ridge, first, we varied the surface tension coefficient γ to examine the sensitivity. A large range of values [0, 0.01, 0.1, 1, 10, 100 dyn/cm] for the surface tension coefficient γ were investigated. Surface tension coefficient is generally much bigger than 0.01 dyn/cm and 0.1 dyn/cm for the polymer solutions we studied, typically in the range of 40 to 80 dyn/cm. However, as a theoretical study, we wanted to see how surface tension affects capillary ridge height over a large range.

Figure 2-4 shows the results of changing capillary ridge height (black solid and dotted lines, left axis) and spreading time (red dashed and dash-dot lines, right axis) with different surface tension coefficients γ for both Newtonian ($n=1$) and shear-thinning fluids ($n=0.5$).

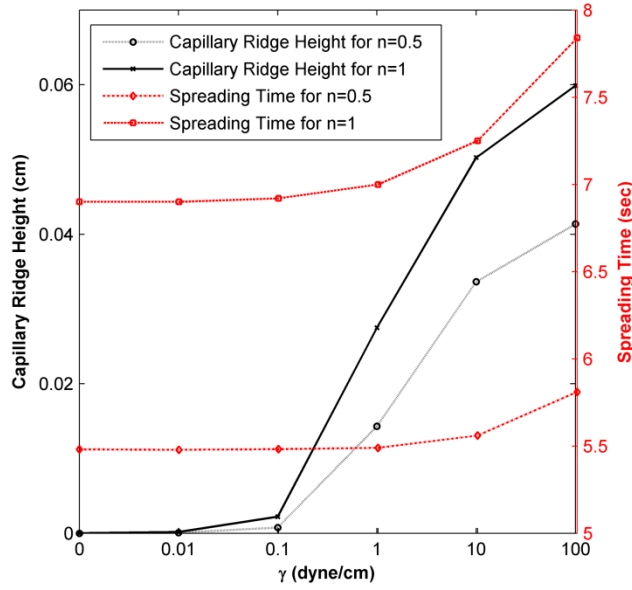


Figure 2-4. Plot of the capillary ridge height h_{cr} (black solid and dotted lines, left axis) and spreading time (red dashed and dash-dot lines, right axis) as a function of surface tension coefficient γ for both Newtonian ($n=1$, solid and dashed lines) and shear-thinning fluids ($n=0.5$, dotted and dash-dot lines). (Parameters used in the simulation: $m=100 \text{ Ps}^{n-1}$, $\alpha=60^\circ$, $H=0.3 \text{ cm}$, $b=0.01 \text{ cm}$)

For both Newtonian and shear-thinning fluids, the capillary ridge height increased with increasing surface tension coefficient. The impact of surface tension on capillary ridge height had a sharper increase in the range of $[0.1, 10] \text{ dyn/cm}$ than in other regions. The figure also showed that the capillary ridge height of a shear-thinning fluid is less sensitive to changes in surface tension than for Newtonian fluids. Moreover, it took longer time for a larger surface tension fluid to reach to $x=4 \text{ cm}$, which means the surface tension can restrain the spreading. In addition, surface tension slowed the shear-thinning fluids more than the Newtonian fluids. In the range of $[0, 0.1] \text{ dyn/cm}$, the surface tension was not very important for both the spreading shape

and time.

We can conclude that an increase in surface tension coefficient will increase the capillary ridge height. So for the rest of this study, we also want to know how capillary ridge height depends on the other parameters: gel consistency m , shear-thinning index n , initial thickness H , and incline angle α , for a constant surface tension coefficient γ . We used $\gamma = 70$ dyn/cm for the rest of the simulations, referring to the surface tension coefficient measured for a hydroxyethylcellulose (Sigma-Aldrich, viscosity average molecular weight, $M_v = 250,000$) polymer solution.

Over many cases of parametric study, we found that gel consistency m affected the capillary ridge very slightly. Therefore, we considered gel consistency as constant for the following simulations as well. We chose $m = 400 \text{ Ps}^{n-1}$, approximately mid-range of consistency for typical gels used in our lab's experiments (range of $[91.95, 506.58] \text{ Ps}^{n-1}$).

In order to better monitor how the capillary ridge height changes with respect to the other three parameters n , H , and α , we set up coupled parametric studies. The approach is to take one of these parameters as a constant and vary the other two parameters as one series of studies. In total, there are three series varying the following parameter sets:

- 1). n and H
- 2). α and H
- 3). n and α

The range for the shear-thinning index n was set to $[0.5, 1]$ at 0.1 increments, which brackets

the range of n values for typical gels used in our experiments. The range for initial thickness H was [0.2, 0.45] cm at 0.05 increments, because 0.5 cm is the biggest thickness to which is still within the lubrication approximation scope. We also varied the inclination angle α from 10° to 90° at 10° increments (5° increments from 10° to 30°).

In total, there are 360 cases involved in this parametric study. For efficiency, these simulations were run on the Bioinformatics cluster at the KU Information and Telecommunication Technology Center (ITTC).

2.3.2.1. Effect of shear-thinning index (n) and initial thickness (H)

Plots of capillary ridge height for the n and H coupled parametric study are shown in Figure 2-5. We can see that the height of the capillary ridge increased for both increased shear-thinning index n and initial thickness H .

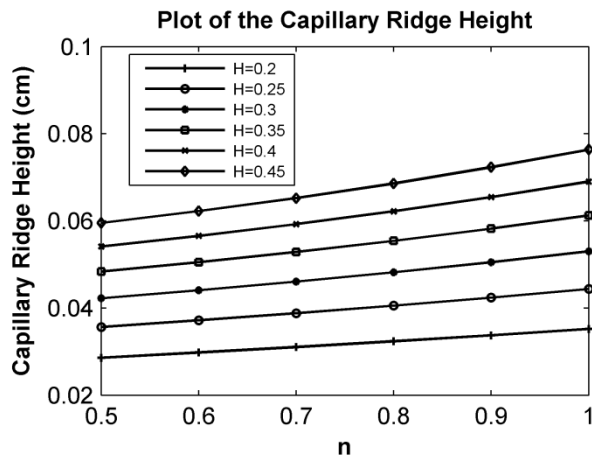


Figure 2-5. Plot of the capillary ridge height h_{cr} (cm) as a function of n for different values of

initial thickness H , with constant $m= 400 \text{ Ps}^{n-1}$, $\alpha=60^\circ$, $\gamma=70 \text{ dyn/cm}$.

First, we compare between Newtonian fluids ($n=1$) and non-Newtonian shear-thinning fluids ($n<1$). If we look at the $H=0.3 \text{ cm}$ line in Figure 2-5 and take the two ends $n=0.5$ and $n=1$ as examples, we can see the difference of the capillary ridge height between the two cases, as shown in the free surface profiles in Figure 2-6. Obviously, a bigger capillary ridge occurred for the Newtonian fluid (red dashed) than for the non-Newtonian fluid (black solid) with the same other parameters. The capillary ridge height is 0.0422 cm for the $n=0.5$ case, and 0.0530 cm for the $n=1$ case.

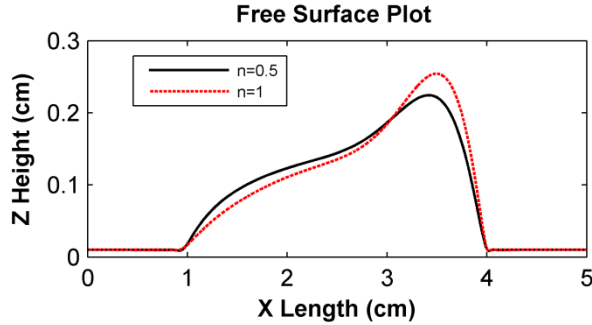


Figure 2-6. Comparison of free surfaces between shear-thinning index $n=0.5$ (black solid) and $n=1$ (red dashed) when gel reaches $x=4 \text{ cm}$, with constant $m= 400 \text{ Ps}^{n-1}$, $\alpha=60^\circ$, $\gamma=70 \text{ dyn/cm}$ and $H=0.3 \text{ cm}$.

Likewise, we can compare between a thicker film and a thinner film – for example, $H=0.2 \text{ cm}$ and $H=0.45 \text{ cm}$ cases at the $n=0.7$ in Figure 2-5. Figure 2-7 shows the difference of the capillary ridge profile between the two cases. We found that the thicker film (red dashed) had a

much bigger ridge than the thinner film (black solid). The capillary ridge height is 0.0311cm for the $H=0.2$ cm case, and 0.0652 cm for the $H=0.45$ cm case.

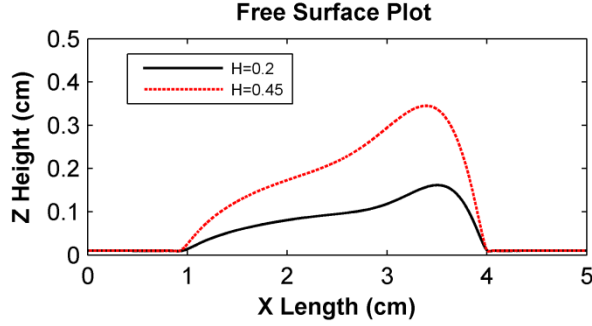


Figure 2-7. (Color online) Comparison of free surfaces between initial thickness $H=0.2$ cm (black solid) and $H=0.45$ cm (red dashed) when gel reaches $x=4$ cm, with constant $m= 400 \text{ Ps}^{n-1}$, $n=0.7$, $\alpha=60^\circ$ and $\gamma=70 \text{ dyn/cm}$.

In summary, increasing shear-thinning behavior reduces the capillary ridge height. Also, a thinner initial thickness will reduce the capillary ridge height as well. In addition, for thicker films, a change in shear-thinning behavior has more impact than for thinner films.

2.3.2.2. Effect of inclination angle (α) and initial thickness (H)

As shown in Figure 2-8, the capillary ridge height is an increasing function for both increasing α and H . Inclination angle α plays a more important role than H , and the inclination angle's impact on the capillary ridge height increased at higher initial thickness. In addition, in the range of $[40^\circ, 90^\circ]$, H starts to have more influence than it does in the range of $[10^\circ, 30^\circ]$. Moreover, in the range of $[5^\circ, 15^\circ]$, the capillary ridge height is very small. An alternate definition of h_{cr} using the

actual ridge height, as well as a side profile plot, indicated insignificant capillary ridge in the range of $[5^\circ, 15^\circ]$. Some previously published studies for Newtonian fluids [16] showed there existed a critical angle where the capillary ridge just started to appear. This implies that we can control the inclination angle in experiments to prevent the appearance of a capillary ridge. In summary, both α and H can be controlled to impact capillary ridge height.

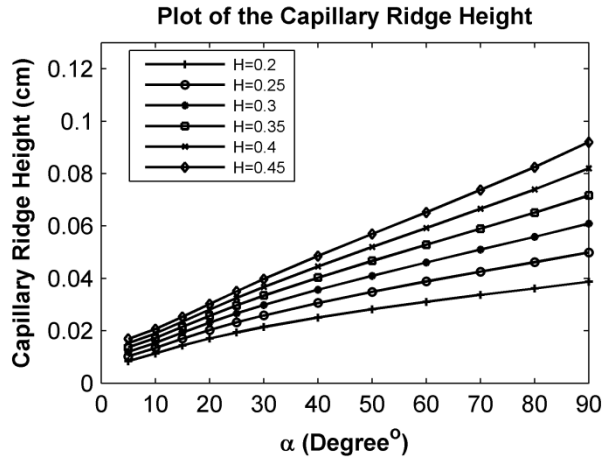


Figure 2-8. Plot of the capillary ridge height h_{cr} (cm) as a function of α for different values of initial thickness H , with constant $m= 400 \text{ Ps}^{n-1}$, $n=0.7$ and $\gamma=70 \text{ dyn/cm}$. Note: a finer mesh between 10° and 40° for α was applied to handle the rapid change.

2.3.2.3. Effect of shear-thinning index (n) and inclination angle (α)

Similarly, Figure 2-9 shows the capillary ridge height is an increasing function for both increasing n and α . In other words, as the fluid becomes more Newtonian or is on a steeper incline, the capillary ridge gets bigger. Inclination angle α has more influence on the capillary ridge height than n . At greater inclination angles, shear-thinning behavior has a slightly greater impact than at smaller inclination angles. In summary, both changes in inclination angle and

shear-thinning index can be used to control the capillary ridge height of a film, but the inclination angle has much greater influence.

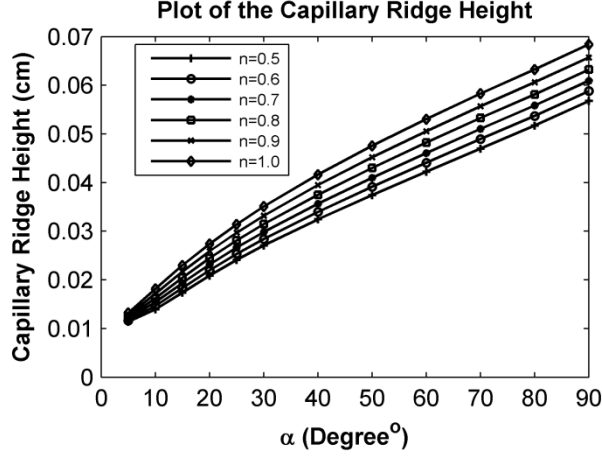


Figure 2-9. Plot of the capillary ridge height h_{cr} (cm) as a function of α for different values of n , with constant $m=400 \text{ Ps}^{n-1}$, $H=0.3 \text{ cm}$ and $\gamma=70 \text{ dyn/cm}$. Note: a finer mesh between 10° and 40° for α was applied to handle the rapid change.

2.4. Conclusions

In summary, according to our numerical model of spreading of power-law fluids on an incline, surface tension effect influences both the spreading shape and speed of the fluid. The dramatic difference between this surface tension model and the previous model is the capillary ridge at the front of the gel. We found in our parametric analysis that capillary ridge height is an increasing function of surface tension coefficient γ , inclination angle α (when $\alpha > \text{critical angle}$), initial thickness H , and shear-thinning index n . We also found that gel consistency m affects the

capillary ridge very slightly. Furthermore, a fluid flows slower if the surface tension coefficient γ increases.

In addition, our parameter analysis provided some useful conclusions about the relative impact of the parameters on capillary ridge height. The capillary ridge height of a shear-thinning fluid is less sensitive to changes in surface tension than for Newtonian fluids. In thicker films, a change in shear-thinning behavior has more impact than it does for thinner films. Inclination angle plays a more important role than initial thickness, and the angle's impact is greater for thicker films. Initial thickness has a greater influence at steeper angles than flatter angles. There exists a critical angle where the capillary ridge just started to appear. Inclination angle also has a greater impact than shear-thinning behavior. But at steeper angles, shear-thinning behavior has a little more influence than at flatter angles.

All of these conclusions directly inform the experimental design for our planned experimental analysis of these flows, (refer to Appendix E for details). These conclusions are also very important because we can use them to optimize a polymer solution's properties for optimal flow and surface coverage. The literature suggests that the emergence of a capillary ridge may indicate fingering instabilities at the spreading front [16]. In our specific application in microbicide coating of epithelial surfaces, fingering instabilities during epithelial coating may change the microbicide gel distribution and impact how well it can protect the epithelium. Therefore, our study indicates we can control the inclination angle or optimize the shear-thinning index n to prevent the appearance of the fingering instabilities. For example, inclination angle

results could be translated to package instructions for posture during microbicide gel application by the user. Additionally, gel structure or components could be altered to yield rheological parameters for optimal spreading with no fingering. The utility of this study's conclusions is not limited to drug delivery applications. The results are applicable to other fields where gravity-driven thin film flows of shear-thinning fluids are present.

3. CONTACT LINE INSTABILITY OF GRAVITY-DRIVEN FLOW OF POWER-LAW FLUIDS

The study described in this chapter has been published as Ref. [55]:

Hu, B. and S.L. Kieweg, *Contact line instability of gravity-driven flow of power-law fluids*.

Journal of Non-Newtonian Fluid Mechanics, 2015. 225: p. 62-69.

3.1. Introduction

Gravity-driven thin film flow with fingering instability is of interest in many fields, such as industry (paints [10], contact lens manufacture [11], and microchip fabrication [12]), nature (lava flow [13] and glacier flow [14]), and biomedical applications (microbicidal drug delivery [35, 56], eye tears and substitutes [57]). In many applications, a uniform coating is desired with no dry spots. Thus, it is very important to understand the mechanics of fingering instability at the moving contact line of a spreading thin film.

Numerous experimental and analytical/numerical studies have examined the dynamics of a gravity-driven contact line following the famous study of Huppert [58]. Schwartz [44] proved that contact line instability is controlled by surface tension effects. Troian et al. [43] carried out linear stability analyses (LSA) on thin film flow and derived the formulation under the limit of small wavenumber to show that the capillary ridge was responsible for the instability. Bertozzi and Brenner [16] verified the LSA numerically and developed the transient model to investigate the transient growth of the fingering instability. Lin and Kondic [47] studied the instability of the

thin films flowing down an inverted incline. These studies all assumed a constant flux configuration, however, in practical applications, a constant-volume configuration is often needed. In our previous 2D study [35], we showed how the capillary ridge at the front of the flow evolves for a constant volume configuration. Espin and Kumar developed a 2D constant-volume model to study the thin film flow of colloidal suspensions, and showed that both particle concentration and evaporation have a large impact on a front interface [59, 60]. Gonzalez et al. and Gomba et al. developed predictive models and integral method to study the linear stability of constant volume flow [49, 50]. All of these studies provide a systematic approach to deal with the capillary ridge and contact line instability problem.

However, most of those previous studies were for Newtonian fluids. The fluids used in the above mentioned industrial and biomedical applications usually exhibited non-Newtonian behavior, especially shear-thinning behavior. There are few published studies on contact line instability of non-Newtonian fluids. Balmforth *et al.* [48] studied the instability of Bingham fluids using LSA and showed that yield stress stabilized the contact line. Spaid and Homsy [61, 62] used energy analysis for viscoelastic fluids to show that elasticity has a stabilizing effect on the capillary ridge. It is still unknown how shear-thinning behavior for non-Newtonian fluids can affect contact line instability.

In chapter 1 [35], we completed a 2D analysis of shear-thinning fluids. Using travelling waves and numerical simulations of one-dimensional spreading, we found that increasing the shear-thinning behavior of polymer solutions decreased the capillary ridge height. This leads to

the hypothesis for this study: that more shear-thinning fluids should have suppressed finger growth and longer finger wavelengths, and that this should be evident in linear stability analysis and 3D numerical simulations. In summary, the relationship between the emergence and height of a capillary ridge in a 2D shear-thinning model has not previously been related to linear stability analysis and the 3D numerical model of contact line instability. To solve this issue, it is important to develop a contact line model of power-law fluids and to identify the importance of different factors affecting fingering instability.

To verify the linear stability analysis of a Newtonian fluid, Kondic and Diez [15, 24, 41, 45, 46] numerically studied the 3D flow needed to simulate fingering instability in the transverse direction. Lin et al. [63] studied 3D simulations for fluids on an inverted incline for unevenly distributed fluid viscosity. Those studies were also only for Newtonian fluids. Our research group has developed a 3D model for power-law fluids [64] and Ellis fluids [31] to study the spreading speed of a polymeric solution and compared the results with experiments. However, those models did not incorporate surface tension effect, and therefore cannot simulate fingering instability.

The goals of this study are to: (a) develop a contact line model using LSA (section 3.2), and study how the shear-thinning effect would influence the finger growth, and (b) expand to 3D flow simulations with various perturbations in order to verify the LSA results (Section 3.3).

3.2. Linear stability analysis

3.2.1. Methods of linear stability analysis

The fluid is described by the power-law constitutive model [29] :

$$\tau_{ij} = m |II_{2D}|^{\frac{n-1}{2}} (2D_{ij})$$

where $\tilde{\tau}$ is the stress tensor, m is the consistency of the power-law fluid, $2\tilde{D} = (\nabla\tilde{v})^T + \nabla\tilde{v}$ is the shear rate tensor, \tilde{v} is the velocity vector, and $II_{2D} = (1/2) \left[(tr 2\tilde{D})^2 - tr (2\tilde{D})^2 \right]$ is the second invariant of the shear rate tensor.

To describe the movement of the fluid's free surface flow down an incline, a wetting flow assumption and the thin film lubrication approximation are commonly used. A non-dimensional partial differential equation (PDE) for the 3D flow (i.e., 2D spreading) of power-law fluids can be obtained for the height of the fluid as a function of space and time, $h(x, y, t)$. A similar detailed derivation was shown in Perazzo and Gratton [52] and our previous publications on power-law models [35, 64]. We used similar approach to non-dimensionalize the 3D evolution equation as we did for the 2D one in Chapter 2, refer to detailed derivation in Appendix D. The resulting non-dimensional thin film equation for a power-law fluid is:

$$\begin{aligned} \frac{\partial h}{\partial t} + \frac{\partial}{\partial x} \left\{ h^{\frac{1}{n}+2} \left\{ \left[1 - D \frac{\partial h}{\partial x} + \frac{\partial(\Delta h)}{\partial x} \right]^2 + \left[D \frac{\partial h}{\partial y} - \frac{\partial(\Delta h)}{\partial y} \right]^2 \right\}^{\frac{1}{2n}-\frac{1}{2}} \left[1 - D \frac{\partial h}{\partial x} + \frac{\partial(\Delta h)}{\partial x} \right] \right\} \\ - \frac{\partial}{\partial y} \left\{ h^{\frac{1}{n}+2} \left\{ \left[1 - D \frac{\partial h}{\partial x} + \frac{\partial(\Delta h)}{\partial x} \right]^2 + \left[D \frac{\partial h}{\partial y} - \frac{\partial(\Delta h)}{\partial y} \right]^2 \right\}^{\frac{1}{2n}-\frac{1}{2}} \left[D \frac{\partial h}{\partial y} - \frac{\partial(\Delta h)}{\partial y} \right] \right\} = 0 \end{aligned} \quad (1)$$

where n is the power-law index and $n < 1$ indicates shear-thinning fluids. The dimensionless parameter $D = \cot\alpha(C_a)^{1/3}$ reflects the magnitude of the normal component of gravity force (e.g., $D = 0$ is vertical, $D = 1$ is inclined). The dimensionless parameter $C_a = \mu_0 U / \gamma$ is the power-law capillary number, α is the inclination angle, and γ is the surface tension coefficient. U is a characteristic velocity and μ_0 is a characteristic viscosity incorporating the power-law terms. These latter terms follow the dimensionless groups used for Newtonian fluids [15, 16], and were further modified for the power-law variation as described in more detail in Appendix D.

To conduct a linear stability analysis (LSA), we first determine a traveling wave solution. The method described here for traveling waves and LSA follows the general approach described in detail for Newtonian fluids by previous authors, e.g., in [15, 16]. To find a traveling wave solution, we assume $h(x, y, t)$ is y -independent to reduce Eq. (1) to its 2D form. Then, we assume constant flux boundary conditions such that the fluid height is flat far from the moving front: $x \rightarrow -\infty, h \rightarrow 1$ and $x \rightarrow \infty, h \rightarrow b$, where $b \ll 1$ is the thickness of the precursor. This boundary condition leads to a traveling wave solution $h_0(x, t)$ in the x -direction. Using a moving reference frame, $x^* = x - Ut$ traveling with velocity U , the following ODE for $h_0(x^*, t)$ is obtained (dropping $*$ from here forward)

$$-Uh_0 + \left\{ h_0^{\frac{1}{n}+2} \{ [1 - D(h_0)_x + (h_0)_{xxx}]^2 \}^{\frac{1}{2n}-\frac{1}{2}} [1 - D(h_0)_x + (h_0)_{xxx}] \right\} = f \quad (2)$$

where the boundary conditions also result in the following expressions

$$U = \frac{1-b^{\frac{1}{n}+2}}{1-b}, \quad f = \frac{-b+b^{\frac{1}{n}+2}}{1-b}$$

Eq. (2) was numerically solved (see Appendix C) for the traveling wave solution, which may form a capillary ridge. The presence and height of the ridge depends on many factors, such as D and the power-law index, n [35].

Next, we can use this traveling wave solution as the ‘base’ solution in the x direction. When we try to expand to the transverse y direction, we can simply assume the solution is in the form of a base state h_0 with a perturbation h_1 , $h(x, y, t) = h_0(x) + \epsilon h_1(x, y, t)$, where h_0, h_1 are of $O(1)$ and $\epsilon \ll 1$, and substitute it into the thin film PDE (Eq (1)). Only terms that are on the order of ϵ are kept in the resulting equation, and h_1 can be expressed as a Fourier transform using the superposition principle, $h_1(x, y, t) = \int_{-\infty}^0 g(x, t) e^{iqy} dq$, where q is the wavenumber. We apply a Taylor series to expand the power terms in Eq. (1). The Taylor approximation is kept in the same order of ϵ . We also use the traveling wave solution of Eq. (2) to substitute for the higher order terms. After simplification, the PDE for $g(x, t)$ is

$$\begin{aligned} & \frac{\partial g}{\partial t} + \frac{\partial}{\partial x} \left\{ \left[\left(\frac{U h_0 + f}{h_0^{\frac{1}{n}+2}} \right)^{2n} \right]^{\frac{1}{2n}-\frac{1}{2}} \left\{ \left(\frac{1}{n} + 2 \right) h_0^{\frac{1}{n}+1} \left[\left(\frac{U h_0 + f}{h_0^{\frac{1}{n}+2}} \right)^2 \right]^{\frac{n}{2}-\frac{1}{2}} \left[\frac{U h_0 + f}{h_0^{\frac{1}{n}+2}} \right] g + \frac{1}{n} h_0^{\frac{1}{n}+2} [(-q^2 - D) g_x + g_{xxx}] \right\} \right\} \\ & - \left\{ \left[\frac{(U h_0 + f)}{h_0^{\frac{1}{n}+2}} \right]^{2n} \right\}^{\frac{1}{2n}-\frac{1}{2}} h_0^{\frac{1}{n}+2} [q^2 (-Dg - q^2 g + g_{xx})] - U \frac{\partial g}{\partial x} = 0 \end{aligned} \quad (3)$$

The solution of Eq. (3) provides information about the growth of an imposed perturbation, and

how that growth depends on the wavenumber. The growth rate, σ , of $g(x, t)$ is defined from the exponential time dependence of $g = \varphi(x)e^{\sigma t}$ due to the homogeneity of Eq. (3), and that growth rate will be a function of the wavenumber. In the following sections, this PDE is solved using both analytical and numerical methods.

3.2.2.1. Small wavenumber analysis

To obtain an analytical solution of Eq. (3) for $g(x, t)$, we follow the approach in Refs. [15, 43], summarized as follows. We first need to assume that the wavenumber q is small, so we can write

$$g = g_0 + q^2 g_1 \quad (4)$$

and the growth rate is thus

$$\sigma = q^2 \sigma_1 \quad (5)$$

We substitute Eq. (4) and Eq. (5) into Eq. (3), and the second order, $O(q^2)$, terms give

$$\begin{aligned} \sigma_1 \varphi_0 + \frac{\partial}{\partial x} \left(\left[\left[\frac{(U h_0 + f)}{h_0^{\frac{1}{n}+2}} \right]^{2n} \right]^{\frac{1}{2n}-\frac{1}{2}} \left\{ \left(\frac{1}{n} + 2 \right) h_0^{\frac{1}{n}+1} \left\{ \left[\frac{(U h_0 + f)}{h_0^{\frac{1}{n}+2}} \right]^2 \right\}^{\frac{n}{2}-\frac{1}{2}} \left[\frac{(U h_0 + f)}{h_0^{\frac{1}{n}+2}} \right] \varphi_1 + \frac{1}{n} h_0^{\frac{1}{n}+2} [-\varphi_{0,x} - D\varphi_{1,x} + \varphi_{1,xxx}] \right\} \right) \\ - \left\{ \left[\frac{(U h_0 + f)}{h_0^{\frac{1}{n}+2}} \right]^{2n} \right\}^{\frac{1}{2n}-\frac{1}{2}} h_0^{\frac{1}{n}+2} [(-D\varphi_0 + \varphi_{0,xx})] - U\varphi_{1,x} = 0 \end{aligned} \quad (6)$$

We can integrate Eq. (6) over the domain in x $[-\infty, 0]$, and substitute φ_0 for $h_{0,x}$. After applying the traveling wave solution and $\varphi_1 \rightarrow 0$ at the boundary, we obtain the growth rate as a function of a base solution, h_0 :

$$\sigma_1 = \int_{-\infty}^0 h_0(h_0^{1+n} - 1)dx \quad (7)$$

Note, we assume precursor $b = 0$ to further simplify the problem, and directly compare to the result for Newtonian fluids in Ref. [15].

Eq. (7) is used in this small wavenumber analysis to show why the capillary ridge examined in our previous 2D study [35] is important. When the base solution has a capillary ridge (i.e., $h_0(x) > 1$), Eq. (7) indicates that the growth rate is positive, and thus the contact line is unstable. If the growth rate is negative, the perturbation does not grow, and the fingering instability is suppressed. This conclusion from Eq. (7) for shear-thinning fluids is consistent with the studies for Newtonian fluids [15, 43]. The conclusion of this analytical solution for small wavenumbers connects this LSA analysis to our previous 2D model [35], where we investigated how the capillary ridge is affected by the shear-thinning effect and D , which in turn impact the base solution and thus growth rates. To completely and further examine the impact of these terms on the growth rate, we numerically solved Eq. (3) for all wavenumbers as described in the next section.

3.2.2.2 Numerical approach

Following the procedure outlined by Kondic [15] for Newtonian fluids, the PDE for $g(x,t)$ (Eq. (3)) for arbitrary perturbation wavenumbers can be numerically solved using the following steps:

1. Obtain the traveling wave base solution, $h_0(x)$, using numerical methods for a constant-flux condition (as in our previous 2D power-law study [35]).
2. For a given wavenumber q and known base solution, $h_0(x)$, the PDE for $g(x,t)$ (Eq. (3)) can be solved numerically. We developed a C code to solve the PDE (Eq. (3)) using an implicit finite difference scheme. We applied the Crank–Nicolson method for the time derivative and central difference for the space derivatives. Newton’s method was used to solve the algebraic equations resulting from finite difference discretization.
3. Once $g(x,t)$ is obtained, the growth rate σ as a function of wavenumber can be calculated by assuming $g(x,t)$ depends exponentially on time using:

$$\sigma = \frac{1}{g} \frac{\partial g}{\partial t}$$

4. Solve for other q values for all modes by repeating 2-3, and plot growth rate σ as a function of wavenumber q .

3.2.2. Results and discussion: LSA

Figure 3-1 shows the LSA results for Newtonian ($n = 1$) and shear-thinning fluids

($n = 0.6, 0.8$). If the growth rate is positive, this indicates that the contact line is not stable. We can see the growth rate is bigger on the vertical plane ($D = 0$) than for the less-inclined planes ($D = 0.5$ and 1) for all three fluids. Also, the growth rates are larger for Newtonian fluids than shear-thinning fluids. For $D = 2$, the growth rate is never positive, indicating that fingering instability is suppressed. The Newtonian results agree with the existing studies in the literature [15, 16]. It is interesting to see the most unstable wavenumbers for all three types of fluids on the vertical plane ($D = 0$) are the same, while for the flatter planes ($D = 0.5$ and 1), the most unstable wavenumbers for shear-thinning fluids are smaller than for the Newtonian fluid. We will further discuss this in section 3.3, in conjunction with the 3D results.

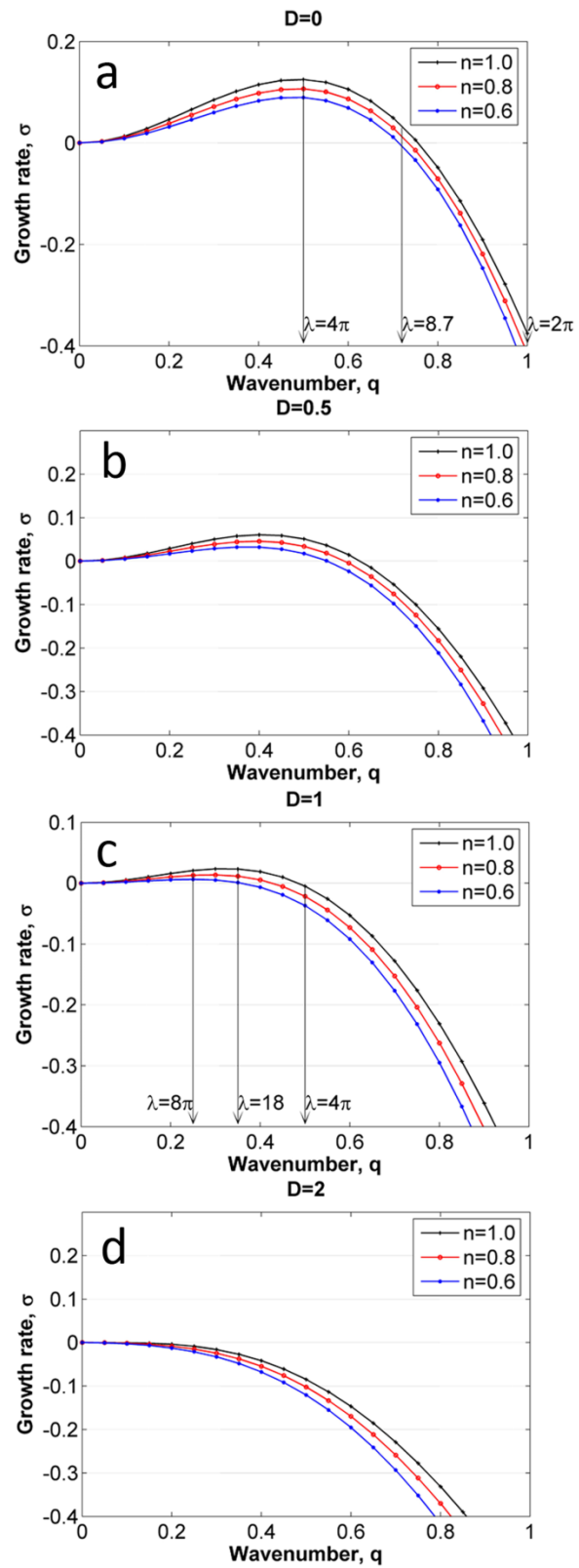


Figure 3-1. The LSA growth rate as a function of wavenumber q and power-law index n . Comparison among different dimensionless numbers: $D=0$ (a), $D=0.5$ (b), $D=1$ (c) and $D=2$ (d). Figures (b), (d) and the vertical lines in Figures (a) and (b) will be discussed later in Section 3.3 in conjunction with 3D simulations. (Other simulation parameters: precursor $b=0.1$, $\Delta x=0.01$, $\Delta t=0.01$.)

The impact of the precursor thickness on fingering instability has been investigated in previous studies for Newtonian fluids. Both numerical [16, 50] and experimental [65] studies indicated that increasing the thickness of the precursor can suppress fingering instability of Newtonian fluids. The growth rate curves of a shear-thinning fluid ($n = 0.8$) shown in Figure 3-2 indicate that the same trend holds for the power-law fluid. As the precursor thickness increases, the growth rate decreases.

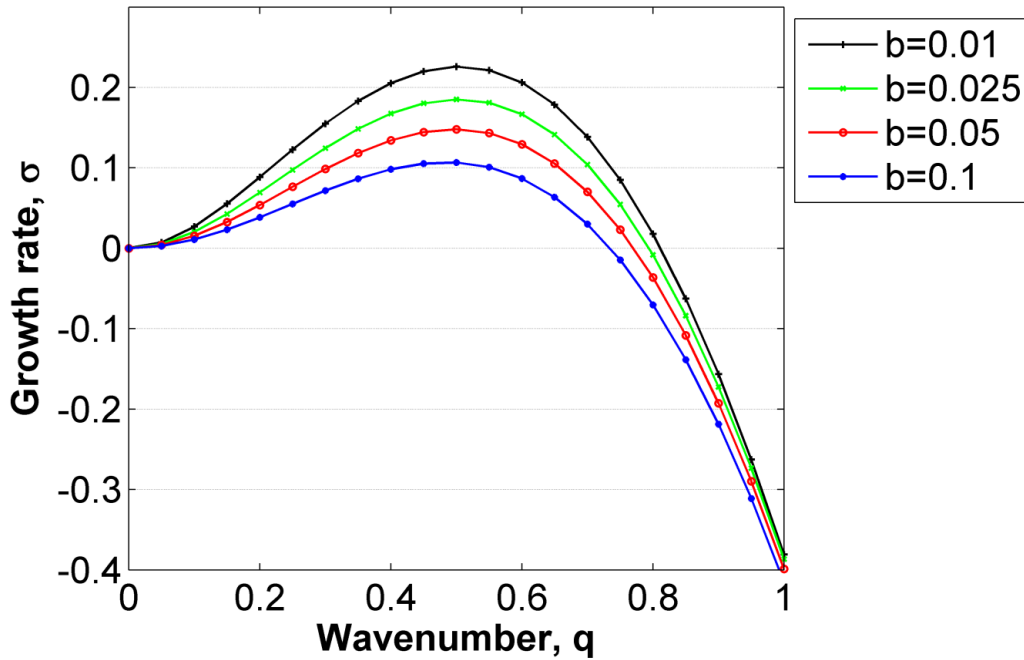


Figure 3-2. Effect of precursor thickness on LSA growth rate for a shear-thinning fluid: $b=0.01$ (black solid), $b=0.025$ (green dotted), $b=0.05$ (red circled), and $b=0.1$ (blue dotted). (Other simulation parameters: $n=0.8$, $D=0$, $\Delta x=0.01$, $\Delta t=0.01$)

In our previous 2D study [35], we found that capillary ridge height increases with increasing power-law index n , but decreases with increasing precursor thickness b . Those conclusions match these LSA results very well. This numerically shows that capillary ridge is directly related to contact line fingering instability, which is consistent with the analytical analysis in Section 2.1.1.

3.3. 3D simulations

To further study fingering instability, we decided to expand to the third, transverse direction and numerically solve the 3D thin film PDE (Eq (1)). The Finite Element Method (FEM) was used for this part of the study. A finite element solver, Dolfin [66], was used for automated assembly of the variational forms of the thin film equation (Eq (1)) over the computational domain. Some other libraries used in this study along with Dolfin are components of the open source FEniCS Project [67].

3.3.1. Finite element formulation

The weak form of the equations can be derived from Eq. (1) as follows:

$$\int q h d\Omega - \int q h' d\Omega + \Delta t \int q \left[\frac{\partial}{\partial x}(T) - \frac{\partial}{\partial y}(K) \right] d\Omega - \int U \frac{\partial h}{\partial x} d\Omega = 0$$

$$\int v T d\Omega - \int v h^{\frac{1}{n}+2} \left\{ \left[1 - D \frac{\partial h}{\partial x} + \frac{\partial C}{\partial x} \right]^2 + \left[D \frac{\partial h}{\partial y} - \frac{\partial C}{\partial y} \right]^2 \right\}^{\frac{1}{2n} - \frac{1}{2}} \left[1 - D \frac{\partial h}{\partial x} + \frac{\partial C}{\partial x} \right] d\Omega = 0$$

$$\int p K d\Omega - \int p h^{\frac{1}{n}+2} \left\{ \left[1 - D \frac{\partial h}{\partial x} + \frac{\partial C}{\partial x} \right]^2 + \left[D \frac{\partial h}{\partial y} - \frac{\partial C}{\partial y} \right]^2 \right\}^{\frac{1}{2n} - \frac{1}{2}} \left[D \frac{\partial h}{\partial y} - \frac{\partial C}{\partial y} \right] d\Omega = 0$$

$$\int o C d\Omega + \int \nabla o \cdot \nabla h d\Omega = 0$$

where q , v , p and o are test functions, and h' is from the previous time step.

3.3.2. Numerical parameters

As shown in Figure 3-3, the flow is from left to right along the x -direction. The boundary conditions in the flow direction are implemented as:

$$h(0, y, t) = 1, \quad h_x(0, y, t) = 0$$

$$h(L_x, y, t) = b, \quad h_x(L_x, y, t) = 0$$

where L_x is the dimensionless length of the computational domain. In the lateral y -direction, a periodic boundary condition is specified at $y = 0$ and $y = L_y$:

$$h(x, 0, t) = h(x, L_y, t)$$

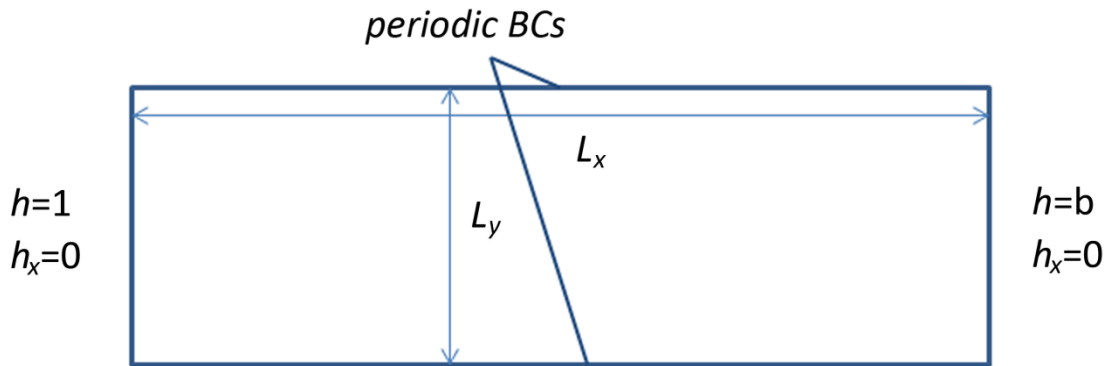


Figure 3-3. Schematic of the boundary conditions (BCs) for the 3D numerical simulation. The subscript on h indicates derivative. Flow is in the x -direction downhill to the right, and the domain width is L_y in the y -direction. The constant flux condition is the non-dimensional $h = 1$ at $x = 0$ for all time. The precursor boundary condition is indicated with $h = b \ll 1$ at the domain boundary $x = L_x$ for all time.

For the initial condition, we used a step function similar to our 2D [35] and LSA studies (see Section 3.2): $h = 1$ at $x = [0, \frac{L_x}{2}]$, and $h = b$ at $x = [\frac{L_x}{2}, L_x]$. To ease the simulation, the step function for the initial profile is smoothed as follows:

$$h(x, y, 0) = \text{Max}\left(\frac{1}{1 + \exp\left(-4\left(x - \frac{L_x}{2}\right)\right)}, b\right)$$

To impose a perturbation at the contact line, we substitute $x = x_0 - 0.2\cos(2\pi y/\lambda)$ into the above equation, so the contact line is slightly convex into the flow direction, where λ is the single mode wavelength of the perturbation. The width of the computational domain for single mode simulations is set to the specified wavelength of the simulation. To simulate randomly imposed perturbations, we used a 50-mode sinusoidal function to perturb the contact line:

$$x = x_0 - \sum_{i=1}^{50} A_i \cos(2\pi y/\lambda_i)$$

characterized by $\lambda_i = 2L_y/i$, where $i = 1, 2, \dots, 50$ and $L_y = 96$. The amplitudes A_i of the sinusoidal functions are random numbers from $[-0.2, 0.2]$.

All 3D simulations were performed on a Lagrange linear polynomial space with continuous Galerkin method, using element sizes of $\Delta x = \Delta y = 0.2$. For the time space, we used the Crank–Nicolson method with $\Delta t = 0.01$. Both the spatial mesh size and the time step were determined through convergence studies and consideration of computational run time.

3.3.3. Results and discussion: 3D simulations

3.3.3.1. Comparison with LSA

In this section, we test three perturbation wavelengths on both a Newtonian fluid ($n = 1$) and shear-thinning fluid ($n = 0.6$) to compare with the LSA results presented in Section 2. Both the vertical plane case ($D = 0$) and less-inclined plane case ($D = 1$) are investigated in this section. Note, we use a single mode perturbation by making the single wavelength equal to the domain length L_y in the y direction: $\lambda = L_y$.

$D = 0$ Case:

We first show the simulation results for the vertical plane. Three wavelengths of perturbation are chosen for this series of simulations and are indicated with vertical lines in the LSA results for $D = 0$ (Figure 3-1a): $\lambda = 4\pi$, 8.7, and 2π . These were selected because the growth rates for the Newtonian fluid ($n = 1$) and shear-thinning fluid ($n = 0.6$) are either both positive at $\lambda = 4\pi$ or both negative at $\lambda = 2\pi$. $\lambda = 8.7$ was selected because the Newtonian fluid has the positive growth rate, whereas the shear-thinning fluid's growth rate approaches zero.

Figure 3-4 demonstrates the results of the 3D simulations over time with $\lambda = 4\pi$, 8.7, and 2π wavelengths. For the top three cases (both Newtonian and shear-thinning fluids cases at $\lambda = 4\pi$, Newtonian fluid case at $\lambda = 8.7$), the perturbed contact lines evolved into growing fingers. This matches the LSA results in Figure 3-1a, which indicate that growth rates for these three cases are greater than zero. The simulations in Figure 3-4 also show that the perturbations of the

Newtonian fluid ($n = 1$) grows faster than these of the shear-thinning fluid ($n = 0.6$) for $\lambda = 4\pi$ and $\lambda = 8.7$. Again, those trends match the LSA results (Figure 3-1a) showing that the growth rate is bigger for Newtonian fluids at these wavelengths. As expected from the negative growth rate for the $\lambda = 2\pi$ LSA results, the perturbations in the bottom two rows of Figure 3-4 are suppressed.

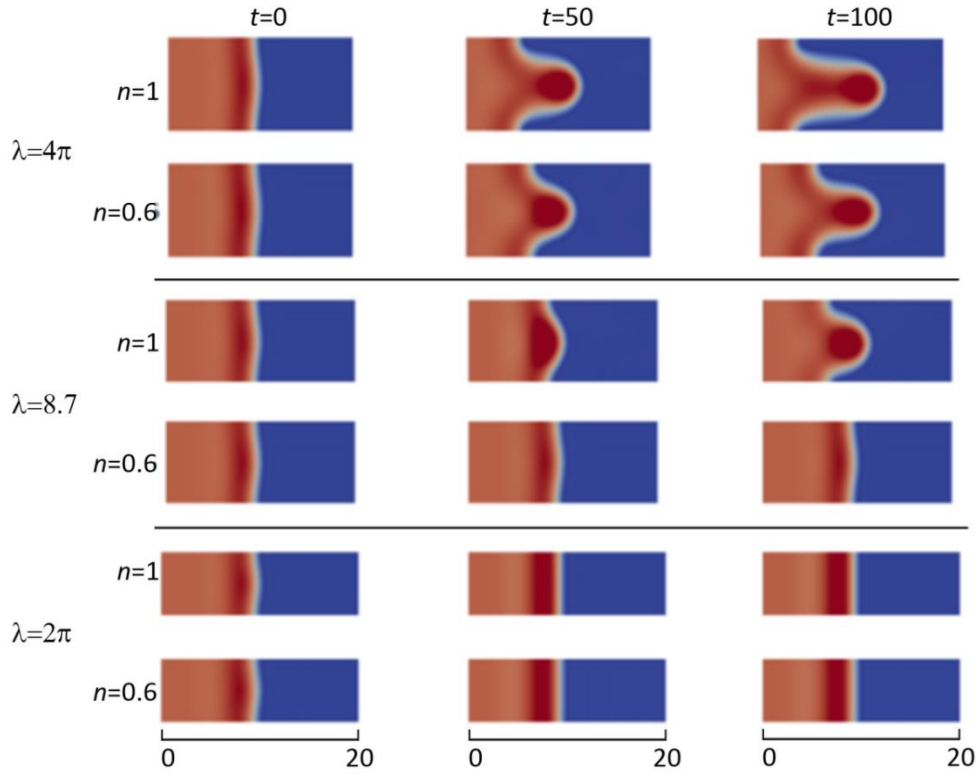


Figure 3-4. Time series of 3D simulations with single mode perturbation, for $D = 0$. Growth of the fingering patterns for both Newtonian (Rows 1, 3, 5) and shear-thinning fluids (Rows 2, 4, 6) on a vertical plane ($D = 0$) with perturbations of different wavelengths $\lambda = 4\pi$, 8.7 , and 2π . From left to right: $t = 0$, 50 , and 100 . $L_x = 20$, $L_y = \lambda$ for each simulation.

$D=1$ Case:

Similar trends and comparisons to LSA can be found on a less-inclined plane ($D = 1$). The LSA results in Figure 3-1c indicate vertical lines at the three wavenumbers selected for analysis here. The corresponding three wavelengths were: $\lambda = 8\pi$, 18 , and 4π . The growth rate for the Newtonian fluid ($n = 1$) and the shear-thinning fluid ($n = 0.6$) are either both positive at $\lambda = 8\pi$ or both negative at $\lambda = 4\pi$. At $\lambda = 18$, only a Newtonian fluid has the positive growth rate, whereas the most shear-thinning fluid's growth rate approaches zero. The 3D simulations for these three single wavelength perturbations are shown in Figure 3-5. The simulations demonstrate that for cases with positive growth rates in the LSA results (Figure 3-1c), all contact lines evolve into fingers (top three rows in Figure 3-5). For those cases with zero or negative growth rates in the LSA results, the contact lines remain unchanged or become flat. In addition, as seen in the vertical case ($D = 0$, Figure 3-4), the contact line of the Newtonian fluid at $D = 1$ is more unstable than that of the shear-thinning fluid.

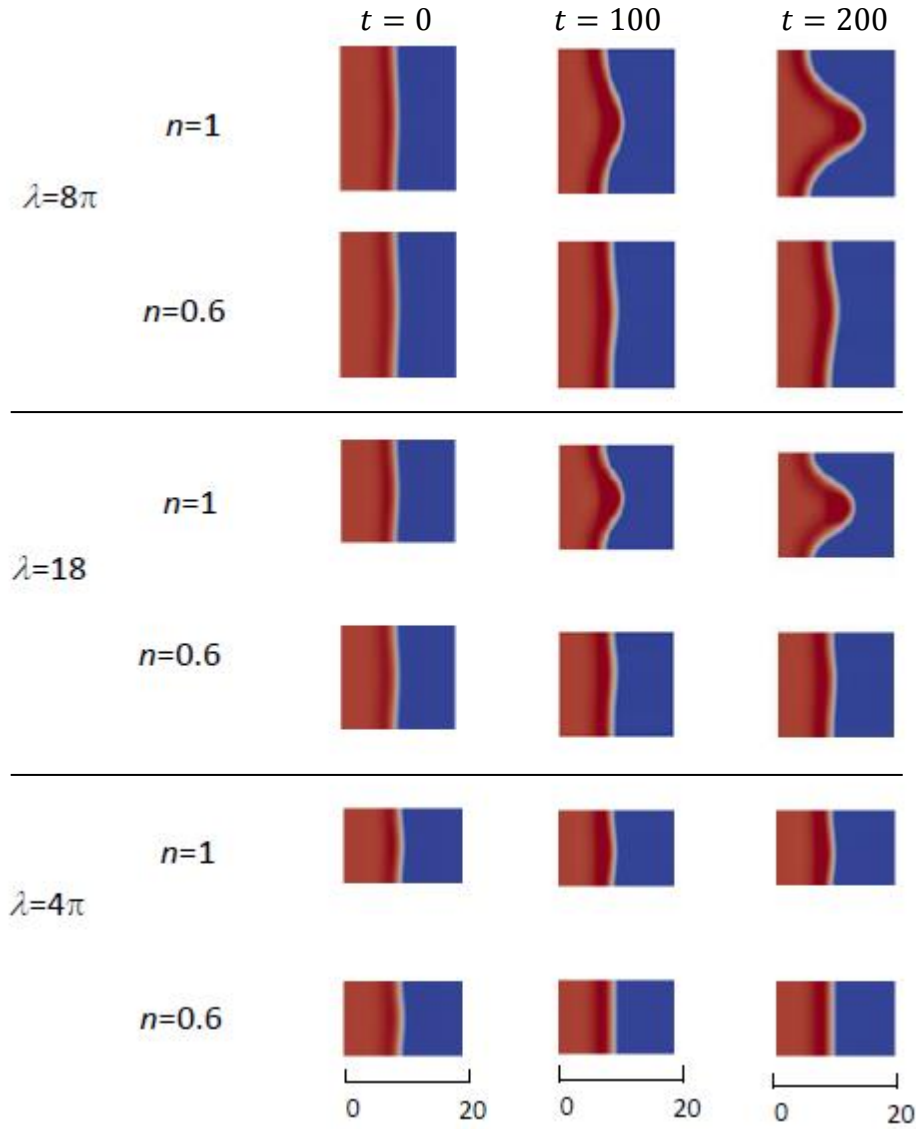


Figure 3-5. Time series of 3D simulations with single mode perturbation, for $D = 1$. Growth of the fingering patterns for both Newtonian (Rows 1, 3, 5) and shear-thinning fluids (Rows 2, 4, 6) on a less-inclined plane ($D = 1$) with perturbations of different wavelengths $\lambda = 8\pi, 18$, and 4π . From left to right: $t=0, 100$, and 200 . $L_x = 20$, $L_y = \lambda$ for each simulation.

However, there is an important difference between the vertical and less-inclined cases. From the LSA results in Figure 3-1, we notice that the corresponding wavelength of the largest growth rate for the vertical case ($\lambda = 4\pi$ for Newtonian) is much smaller than the most unstable

wavelength for the less-inclined case (e.g., $\lambda = 18$ for Newtonian). This trend agrees with published laboratory experiments for Newtonian fluids [15]: the distances between emerging fingers were smaller on a vertical plane than on a less-inclined plane. That trend also occurred for shear-thinning fluids: the most unstable wavelength for the vertical case ($\lambda = 4\pi$ for shear-thinning) is much smaller than the one for the less-inclined case (e.g., $\lambda = 8\pi$ for $n = 0.6$ shear-thinning). The LSA results also show that the most unstable wavelength increases for more shear-thinning fluids, but that is only observed at smaller inclinations. In Section 3.3.3.2 below, we look for the same trends using 3D simulations with multiple mode perturbations, to better simulate a physical experiment.

To further compare growth rates, Figure 3-6 quantitatively compares the growth rate of a finger from 3D simulations and the growth rate of a perturbation from LSA results. The finger length, L , in the simulation is measured from tip to root and is normalized by the initial finger length L_0 from the imposed initial condition. For early times, we can see the growth rate of the finger length from the 3D simulation matches very well with the LSA results. But at later times in the 3D simulation, the finger growth slows and approaches a slower constant speed. This behavior is because at longer times, only a small domain at the front is affected by surface tension. Thus, the overall traveling speed is therefore decided by the traveling wave speed of the constant flux condition. This speed can be calculated using the similarity solution [35]. Similar results for Newtonian fluids can be found in the experimental study in [15], where comparison is made between experimental data and LSA.

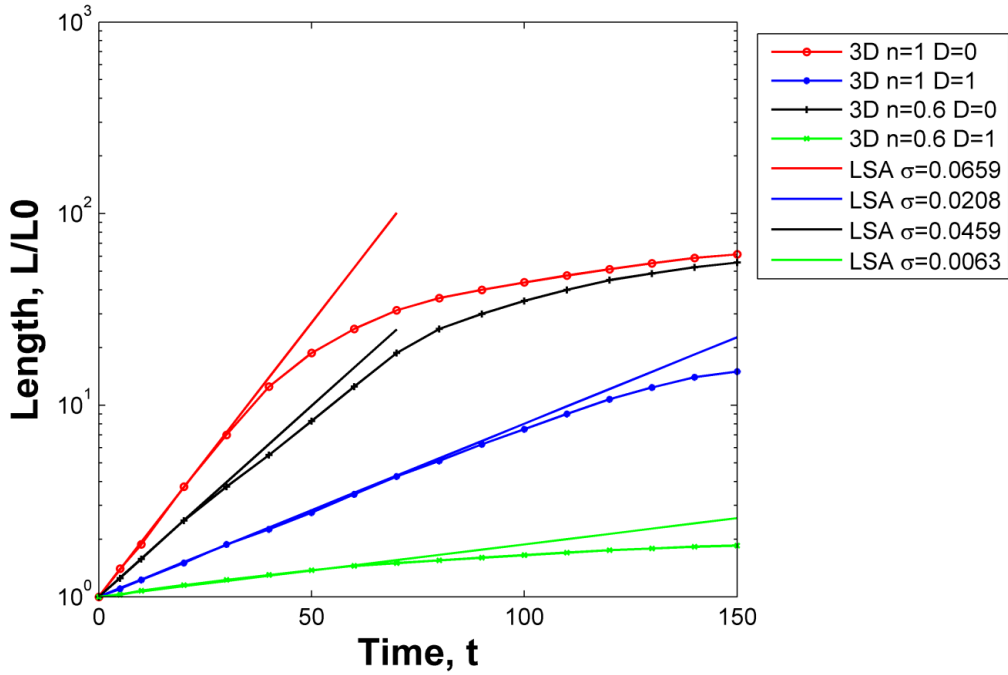


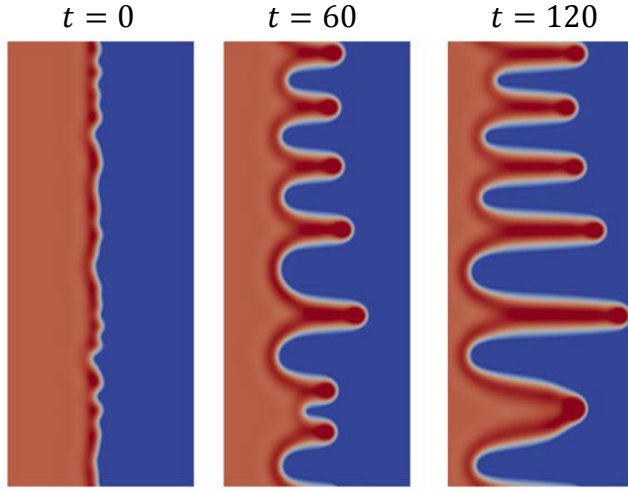
Figure 3-6. Comparison of growth rates from LSA (solid lines) and single mode 3D simulations (symbols). The figure shows the finger length (normalized to initial length) vs. time for four cases: $n = 1, D = 0$; $n = 1, D = 1$; $n = 0.6, D = 0$; and $n = 0.6, D = 1$. For each case, the calculated growth from the 3D simulations (symbols) is compared to LSA prediction (solid lines). (All 3D simulations and LSA results used perturbations of wavelength $\lambda = 8\pi$ which provides a positive growth rate for all simulations.)

3.3.3.2. Simulation of multiple mode, randomly imposed perturbations

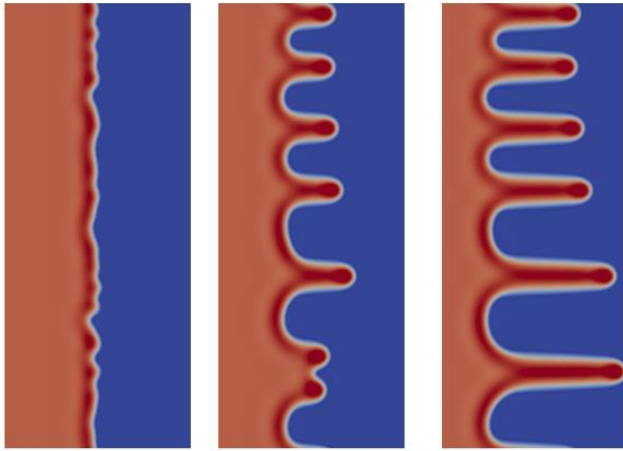
In addition to single mode perturbation, it's also interesting to look at how the contact line is affected by multiple-mode, randomly imposed perturbations. Figure 3-7 shows the $D = 0$ vertical case as an example to demonstrate how the initial perturbed contact line evolves into finger-like rivulets over time a for Newtonian fluid (Figure 3-7a, $n = 1$) and a shear-thinning fluid (Figure 3-7b, $n = 0.6$). The randomly perturbed contact line will corrugate into fingering patterns with similar distances between each finger, for a given simulation. The exceptions are

the areas where two fingers with similar wavelengths merge to form an ‘abnormal’ wider finger.

This can also be observed in our laboratory experiments. An interesting finding is that the merging of the two fingers occurs earlier for the shear-thinning fluid ($n = 0.6$) in Figure 3-7b than for the Newtonian fluid ($n = 1$) in Figure 3-7a. Although two fingers in the Newtonian case emerge at earlier times (not shown), they grow faster and stay independent longer as compared to the shear-thinning fingers, and this makes them more resistant to merging.



(a) $n = 1$



(b) $n = 0.6$

Figure 3-7. Time-series of 3D simulations with multiple-mode, random perturbations for $D = 0$. Comparison between (a) Newtonian $n = 1$ and (b) shear-thinning $n = 0.6$ on a vertical plane ($D = 0$, $L_x = 40$, $L_y = 96$). (Left to right, for $t = 0$, 60, and 120.)

The typical distance between the fingering patterns is related to the most unstable wavenumber in LSA results, according to the existing literature for Newtonian fluids [15, 63]. To check this for shear-thinning fluids, we can use the two $D = 0$ cases in Figure 3-7 to compare

with the LSA results. According to Figure 3-6, LSA results are accurate at early times. Therefore, for the $D = 0$ cases, we chose $t = 60$ for the comparison. From Figure 3-7 at $t = 60$, there are seven fingers (prior to merging) across the width (of 96) at the contact line for both the Newtonian and shear-thinning cases. Therefore the average wavelength is approximately $96/7 \approx 13.7$. That is about 9% different from the most unstable wavelength (4π) for both $n = 1$ and $n = 0.6$, found from the $D = 0$ LSA results shown in Figure 3-1a.

Similar results can be found for the other 3D simulation cases of D and n , and are summarized in Figure 3-8 and Table 3-1. Figure 3-8 compares 3D simulations at one time point for all values of D and n . The times chosen for the contact line patterns in Figure 3-8 are based on the growth rate results shown in Figure 3-6 such that a time point is selected in the range when LSA corresponds to the 3D simulation. Similar to the $D = 0$ case, the average wavelength calculated from 3D simulations matches the most unstable wavelength from LSA results quantitatively. However, unlike the $D = 0$ case, where the average distance between fingers are the same for the three types of fluids, the finger wavelength can vary as a function of shear-thinning for the less-inclined cases. For less-inclined simulations ($D = 0.5$ and 1), the $n = 1$ and 0.8 simulation finger patterns have one more finger than the $n = 0.6$ case. In the simulation for $D = 2$, the flattest inclination, the contact lines are completely stable. This is very apparent in the bottom row of Figure 3-8, and also evident in the LSA results (Figure 3-1d), where the growth rate is negative for all $D = 2$ simulations. Finally, the 3D simulations in Figure 3-8 and comparisons to LSA in Table 3-1 also confirm the results from single-mode

simulations and published Newtonian LSA results: as the inclination approaches vertical, the finger wavelengths are smaller, and the growth rate is faster, and this is true for shear-thinning fluids as well.

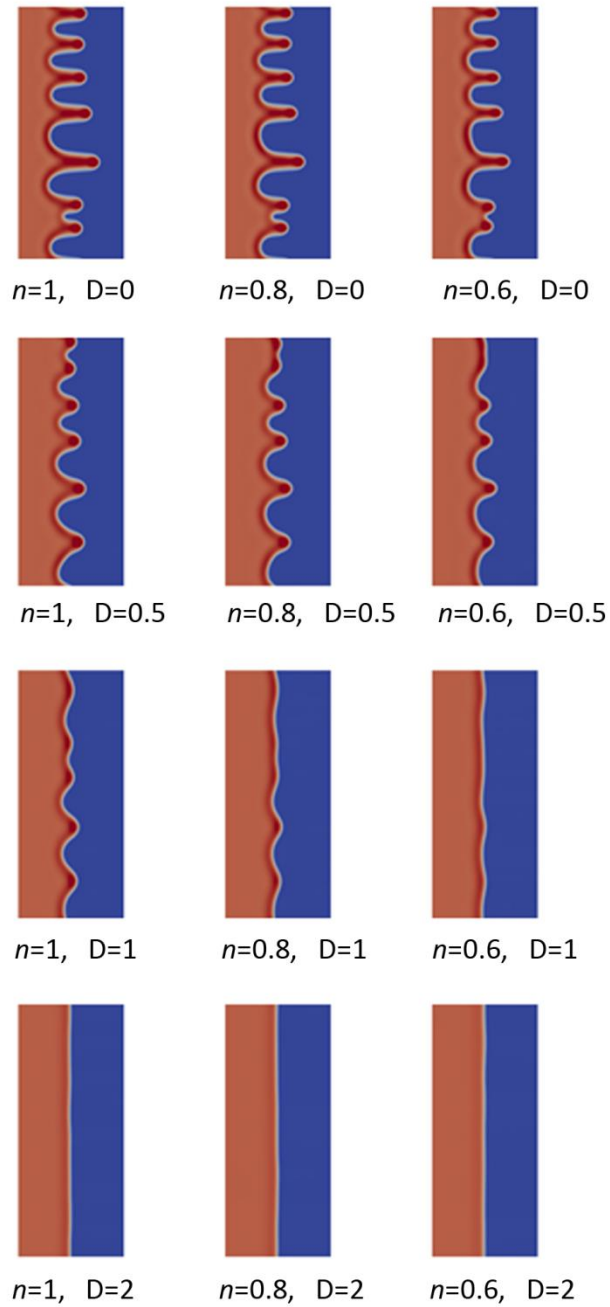


Figure 3-8. A summary of contact line patterns for 12 simulation cases, each showing only one

time point. The points selected were: $t = 60, 80, 100$ and 120 for $D = 0, 0.5, 1$ and 2 , respectively. These time points are in the regime when the LSA results correspond to the linear portion of the 3D numerical simulations in Figure 3-6. ($L_x = 40, L_y = 96$).

$D \backslash n$	0	0.5	1	2
1	$2\pi/0.5=12.566$ <i>$96/7=13.714$</i>	$2\pi/0.4=15.708$ <i>$96/6=16$</i>	$2\pi/0.35=17.950$ <i>$96/5=19.200$</i>	$2\pi/0=\infty$ <i>No finger</i>
0.8	$2\pi/0.5=12.566$ <i>$96/7=13.714$</i>	$2\pi/0.4=15.708$ <i>$96/6=16$</i>	$2\pi/0.3=20.944$ <i>$96/5=19.200$</i>	$2\pi/0=\infty$ <i>No finger</i>
0.6	$2\pi/0.5=12.566$ <i>$96/7=13.714$</i>	$2\pi/0.35=17.952$ <i>$96/5=19.200$</i>	$2\pi/0.25=25.133$ <i>$96/4=24$</i>	$2\pi/0=\infty$ <i>No finger</i>

Table 3-1. A summary of comparison between LSA most unstable wavelength (black – top line of each cell) and 3D characteristic wavelength (italic blue – bottom line of each cell). For the *top line* in each cell, the most unstable wavelength from LSA results (summarized in Figure 3-1a-d for four D values)) was calculated as 2π divided by the wavenumber at the maximum growth rate. For the *bottom line* of each cell, the characteristic wavelength of multi-mode simulations was calculated as the simulation width (96) divided by the number of fingers observed in the simulation. For the vertical case, no difference was observed between Newtonian and the most shear-thinning. For the inclined cases with fingering, the most unstable (LSA) and characteristic (3D) wavelength was longest for the most shear-thinning fluid.

3.4. Conclusions

In summary, the LSA results show that the contact line of a gravity-driven spreading front tends to be more unstable for a vertical plane ($D = 0$) than for a less-inclined plane ($D = 1$). This trend is observed for both Newtonian fluids and power-law fluids. We also found that, for the same conditions, the growth rate for shear-thinning fluids is smaller than that of Newtonian fluids. These findings are further verified in our 3D simulation by comparing the growth rate of the finger length for a single-mode perturbation to the growth rate for the same wavelength in the

LSA results. Simulations with multiple-mode, randomly imposed perturbations showed how fingers with a typical pattern distance are formed. This typical pattern wavelength is considered relevant to the most unstable growth rate in LSA results according to previously published studies for Newtonian fluids. We carried out a parametric study for different D and n and showed that the average distance between finger patterns in our multiple-mode 3D simulations matched the LSA results. We also found that this typical wavelength is the same for both Newtonian and shear-thinning fluids in the vertical case, but is different in the less-inclined cases – the wavelength for a shear-thinning fluid is greater than that for a Newtonian fluid. The multiple-mode 3D simulations also showed the merging of fingers forming atypical patterns commonly observed in actual coating flows and experiments.

Practically, this study can be used in coating flow applications to help avoid the occurrence and/or magnification of the fingering patterns. To improve the coating processes in industrial and biomedical applications, we could optimize the fluid's shear-thinning properties in order to suppress fingering instability and widen finger wavelength. Additionally, since the connection between fingering instability and the capillary ridge was obtained here for shear-thinning fluids, the occurrence of the capillary ridge in our previous 2D model can be used for quick assessment of predicted fingering instability at the contact line. Future studies will use this study as a framework to explore more complex contact line physics and rheological models, such as the Ellis model description of the Newtonian plateau observed at low shear rates in shear-thinning fluids.

4. EFFECT OF VISCOELASTICITY ON SPREADING IN GRAVITY-DRIVEN AND SQUEEZING FLOWS

4.1. Introduction

Microbicide gels are polymeric fluids that exhibit non-Newtonian behavior. Our research group has developed several mathematical tools to understand the flow mechanics in the female vaginal cavity [31, 35, 55, 64]. In those studies including Chapter 2 and 3, we assumed fluids were released on an incline, and used a thin film lubrication approach to simplify the problem. Simpler constitutive models, e.g., power-law and Ellis models, were used due to the shear-thinning rheology of the microbicide gels. However, the spreading speed obtained from previous simulations using these constitutive models didn't match the experimental results well, especially at the early time of the spreading [64]. The early spreading speed was always faster in simulations than that observed in experiments. Since microbicide gels exhibit both viscous and elastic behavior, it is possible that the elastic behavior of the fluid is responsible for differences between previous models and experiments. This is considered as a reasonable assumption, because Khayat also found that gel elasticity may diminish the initial velocity increase for flow inside thin cavities [68]. Very few published studies have been found about the gravity-driven flow of viscoelastic fluids. This is probably because the mathematical modeling of gravity-driven flow with complex constitutive equations is challenging. A few studies were found using simpler

models, e.g., Pavlidis et al. studied the viscoelastic film flow down a vertical cylindrical wall and assumed fully developed flow to avoid modeling the free surface [69].

The first objective of this study was to develop a gravity-driven flow simulation using a more accurate viscoelastic constitutive model. Various viscoelastic constitutive models have been used in recent numerical studies. Favero et al. tested several commonly used constitutive models and their performance for contracting flow [32]. Among these models, Phan-Thien-Tanner (PTT) is considered one of the most realistic models [33]. We used the PTT model for this study.

According to existing literature, to simulate non-Newtonian free surface flow, there are several different approaches. First, there is the thin film lubrication approach we used in the previous studies as in Chapter 2 and 3 [31, 35, 55, 64]. However, using this approach, it is not possible to solve the resulting evolution equation because of the form of the PTT equation. Second, Fourier analysis and a Galerkin projection method are used [70]. However, that approach uses only minimal modes, and it can only be applied to a non-zero initial velocity flow. The most common approach is using free surface models, such as Volume of Fluid (VOF) [71], Level Set [72], and Arbitrary Lagrangian-Eulerian (ALE) [73]. These models require the solution of the full Navier-Stokes equation, therefore they are very accurate and the limitations are fewer compared to the other approaches. Due to the complexity of the problem, we decided to take advantage of the CFD software POLYFLOW [74], which uses the ALE method for free surface modeling.

Besides gravity, squeezing forces from vaginal and underlying tissues also act to distribute and retain the microbicide gels during application. Thus, the second objective of this study is to

model squeezing flow and examine the impact of the viscoelastic behavior of microbicide gels using the same PTT fluid model. Two of our previous studies investigated thin film flow of power-law fluids under the influence of tissue elasticity after gel insertion [25, 75], as shown in Figure 4-1(b) and (c). In those studies, the initial shape of the gel was assumed to be parabolic, and tissue elasticity was incorporated in the pressure term of the momentum equation. The study here focuses on the interaction between the elasticity of the tissue and gel flow during the insertion process, as shown in Figure 4-1 (a) and (b). The objective is to model squeezing flow and examine the impact of the viscoelastic behavior of a microbicide gel and the elasticity of the tissue. In particular, the model will show how the gel is distributed after insertion.

In order to correctly model tissue deformation, we need to couple the PTT flow model with a deformable soft tissue model. Fluid-structure interaction (FSI) models are commonly used for this type of flow. There are no existing FSI studies for vaginal epithelial coating flows according to the authors' knowledge. However, FSI studies are common for blood flow, e.g., Refs. [26-28]. Those types of studies are focused on the effect of the flow on the wall stress for certain tissues in the cardiovascular system, e.g., arteries and heart valves. Due to the complication of the problem and difficulties in solving for the moving interface, most studies use a CFD commercial or open-source packages, e.g., Fluent or SimVascular, and a Newtonian constitutive model or simple shear-thinning models, e.g. power-law and Casson models. In this chapter, we will still use POLYFLOW and its built-in FSI model. It allows coupling of the FSI model with the PTT viscoelastic constitutive model.

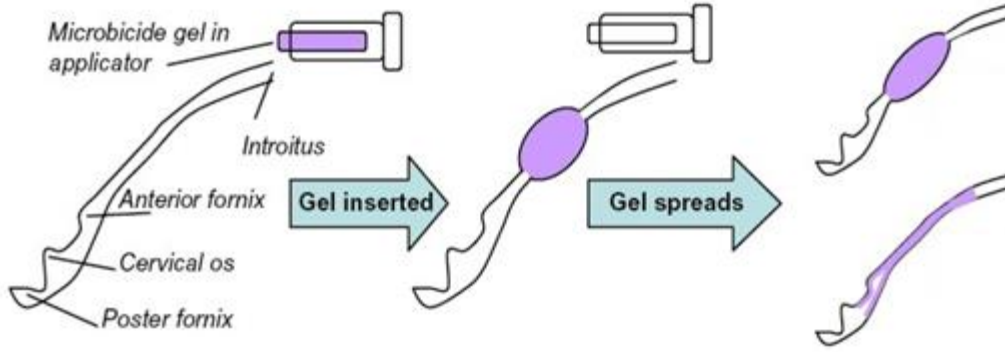


Figure 4-1. Illustration of a microbicide gel applied to the vaginal epithelium and covering of the tissue due to tissue elasticity.

4.2. PTT constitutive model

Section 4.3 and 4.4 will present the gravity-driven flow model and the squeezing flow model.

Here, we describe the viscoelastic model representing the fluid, used in both section 4.3 and 4.4.

To describe the viscoelastic behavior of the microbicide gel, an elastic viscous split stress (EVSS) approach was used to split the stress tensor of the gel, $\boldsymbol{\tau}$, into a Newtonian solvent contribution, $\boldsymbol{\tau}_s$, and an elastic polymeric contribution, $\boldsymbol{\tau}_p$,

$$\boldsymbol{\tau} = \boldsymbol{\tau}_s + \boldsymbol{\tau}_p$$

and the PTT model was considered as the constitutive equation [29],

$$\boldsymbol{\tau}_s = 2\eta_s \mathbf{D}$$

$$\exp\left[\frac{\epsilon\lambda}{\eta_p}(\tau_p)\right]\tau_p + \lambda\left[\left(1 - \frac{\xi}{2}\right)\overset{\nabla}{\hat{\boldsymbol{\tau}}}_p + \frac{\xi}{2}\overset{\Delta}{\hat{\boldsymbol{\tau}}}_p\right] = 2\eta_p \mathbf{D}$$

where λ is the relaxation time, $\overset{\nabla}{\hat{\boldsymbol{\tau}}}_p$ and $\overset{\Delta}{\hat{\boldsymbol{\tau}}}_p$ are the lower and upper convected time derivatives of $\boldsymbol{\tau}_p$, ξ and ϵ are the PTT model parameters, \mathbf{D} is the rate of deformation tensor, and η_s and η_p are

the Newtonian solvent viscosity and polymeric viscosity. The viscosity ratio η_r can be defined as η_s / η , where total viscosity, $\eta = \eta_s + \eta_p$. The objective of this study is to use parametric analysis to determine the effects of these PTT parameters on microbicide gel spreading behavior under either gravity-driven flow or squeezing flow.

4.3. Gravity-driven spreading model

4.3.1. Problem description

We simplified the problem by releasing the gel on an incline to study the flow of gel in response to gravity and viscoelastic effects. Figure 4.2 illustrates the side-profile spreading down an incline. We used a parabolic initial condition to start the flow, which is consistent with our previous gravity-driven flow models. In this study, we focus on how the fluid's viscoelastic behavior affects the spreading length, which describes the spreading speed and how well the gel can cover the target tissue.



Figure 4-2. Illustration of 2D viscoelastic flow down an incline. The side profile of the fluid is shown in dark blue. The white incline is a 60° inclination with respect to horizontal.

4.3.2. Numerical methods

To develop the numerical solution, the first issue is to determine how to track the free surface. We used the Arbitrary Lagrangian-Eulerian method, also called ALE method, in which the computational system is not fixed in space (e.g., an Eulerian representation) or attached to material (e.g., a Lagrangian representation).

We coupled the PTT constitutive equation with the momentum conservation equation and mass conservation equation to solve for the velocity, pressure, stress and strain rate fields, as well

as the mesh nodal positions in POLYFLOW (ANSYS, commercial CFD code).

For the numerical implementation, we used implicit Euler for the integration method. We used quadratic and linear interpolation for velocity and pressure fields, respectively. We also used a Lagrangian method for remeshing and an adaptive meshing method to generate a high quality mesh.

4.3.2. Results and discussion

In this section, a series of simulations was carried out to investigate how the microbicide gel parameters influence the spreading speed of microbicide flow down an incline. The parameters we focused on are relaxation time λ , viscosity ratio η_r , and PTT model parameters ε and ξ . Among these four parameters, the shear-thinning effect is described through ε and ξ . Although they both have elastic and shear-thinning effects, ε is more important in shear free flow, while ξ is more important in shear flow. A non-zero ε leads to a bounded extensional viscosity.

To study the combined effect of these four parameters, we divided them into two groups:

- (1) combined effect of λ , η_r and ε
- (2) combined effect of ε and ξ

The approach is to keep the other parameters constant and only vary the grouped parameters.

Group (1) parameters are considered more important in describing the elastic effect, while Group

(2) parameters convey more information about the shear-thinning behavior.

Parametric analysis 1: Combined effect of λ , η_r and ε

In the first set of results, we studied the parameters that are highly related to the elastic effect. We varied the values of relaxation time λ , viscosity ratio η_r , and PTT parameter ε , and held the other parameters constant. Table 4-1 shows the parametric settings for the first set of simulations. In this section and the next, as a theoretical study, the range of values for these parameters was not limited to the experimental data of microbicide gels. It's interesting to see how these parameters affect the results over a larger range; and therefore, this study can be helpful for more generic fluids. In a later section, we will show some simulations with real curve fitting values of the PTT constitutive equation using rheological data of one of our laboratory polymeric gels.

Case	λ	η_r	ε
1	0.1	0.1	0.01
2	0.1	0.1	0.1
3	0.1	0.2	0.01
4	0.1	0.2	0.1
5	1	0.1	0.01
6	1	0.1	0.1
7	1	0.2	0.01
8	1	0.2	0.1

Table 4-1. Parameter settings for the first set of simulations, where λ is relaxation time, η_r is viscosity ratio, and ε is PTT model parameter, and total viscosity η and PTT parameter ξ are kept as constant, $\eta=200$ P and $\xi=0.01$.

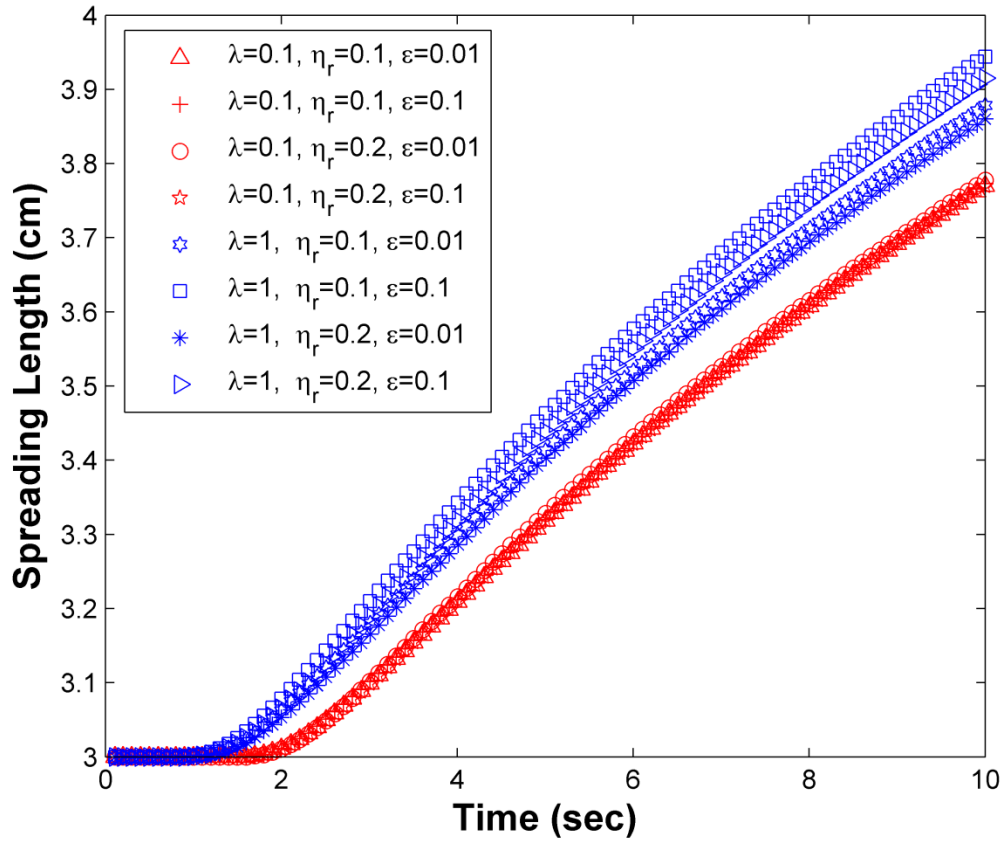


Figure 4-3. Transient result of gravity-driven flow spreading length with varying parameters from Group (1) listed in Table 4-1.

Figure 4-3 shows the results of the parametric cases listed in Table 4-1. In general, spreading length increased with increasing λ and ε , and with decreasing η_r . Relaxation time λ has a larger impact than ε and η_r . At lower λ ($\lambda=0.1$ s), varying ε and η_r doesn't affect the spreading speed much, while at larger λ ($\lambda=1$ s) the gel travels faster with increasing ε , and with decreasing η_r . This means relaxation time is a stronger determinant, and the effects of ε and η_r are highly related to the relaxation time.

Parametric analysis 2: Combined effect of ε and ξ

In this set of results, we studied the effects of ε and ξ , which are more important to the shear-thinning effect. Figure 4-4 shows a multiple-curve plot of spreading length at 10 sec. Noticed that spreading length increases with increasing ε and ξ . They both have more impact in the range of 0.1 to 1. ξ becomes more dominant than ε when they approach 1.

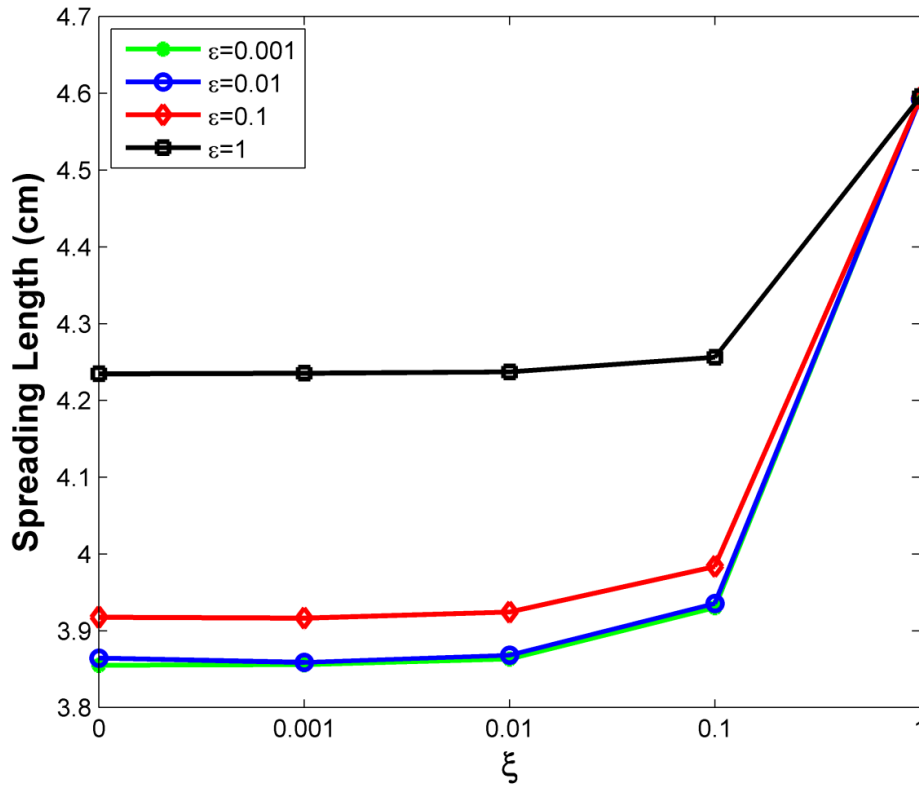


Figure 4-4. Spreading length for different PTT parameters ε and ξ , with constant $\eta=200$ P, $\lambda=1$ s and $\eta_r=0.2$.

Although parametric Groups (1) and (2) results are helpful in showing how sensitive the

spreading speed of the microbicide gels is to the varying values of the PTT parameters, the elastic effect and the viscous effect are not separated satisfactorily. Non-dimensional study and the Deborah number are commonly used for this purpose, identifying whether the viscous effect or the elastic effect dominates the flow. However, Dealy indicated that Deborah number and/or Weissenberg number are only useful under very strict conditions [76]. Due to the nature of the flow in this study, where shear rate and strain rate vary for both position and time, it's impossible to define a characteristic shear rate or observation time. Therefore, dimensionless groups and non-dimensional studies cannot be appropriately used for this work. To answer the question we raised in the introduction section as to the elastic effect being responsible for the discrepancy between power-law simulation results and experiments, we used PTT parameters from rheological data to run simulations.

Simulation results for 2.0 % CMC gel using experimental data

In this section, a real case simulation is performed using our laboratory rheological data [77] for a 2.0 % Sodium carboxymethylcellulose (Blanose 7HF) gel; and results are compared using PTT vs. power-law models. First, the data obtained from experimental measurements of rheology of the CMC gel was curve-fitted. Curve fitting was done using both PTT and power-law constitutive equations. The results are shown in Figure 4-5. The experimental curves are plotted as the dotted curves. They are shear viscosity, η vs. shear rate curve (dotted blue), storage modulus, G' , vs. frequency curve (dotted black) and loss modulus, G'' , vs. frequency

curve. For the PTT model, all three experimental curves are needed. We used a 4-mode model to improve the fitting accuracy. The results are plotted as the solid lines. The coefficients of determination of the fit, R^2 , are 91.82%, 99.01% and 91.55% for the three experimental curves. The 4-mode parameter values are listed in Table 4-2. For the power-law model, only the shear viscosity curve is needed, and the fit is plotted as the dashed blue line. We obtained two parameters from the power-law model curve fitting, gel consistency, $m=125.65\text{Ps}^{n-1}$ and shear-thinning index, $n=0.5059$.

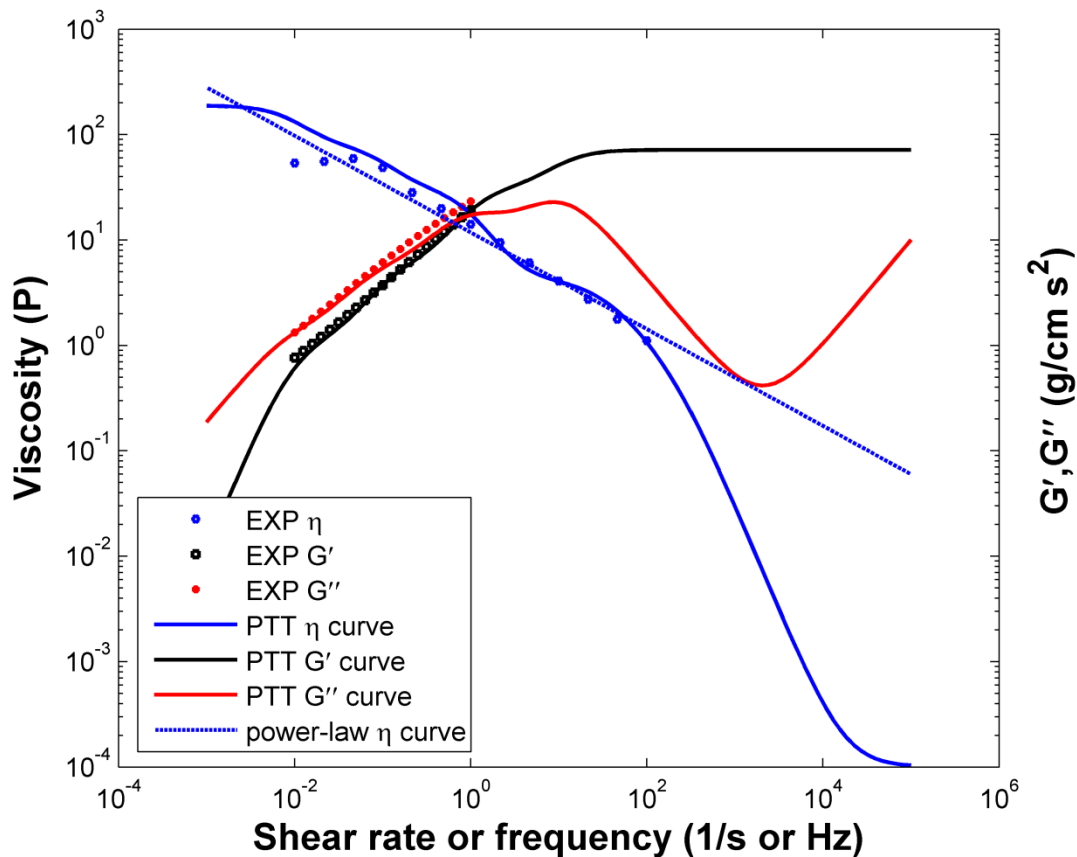


Figure 4-5. Rheological data for a 2.0 % sodium carboxymethylcellulose gel. The dots indicate experimental rheological data, the solid lines show curve-fitting to the PTT constitutive equation, and the dotted line shows curve-fitting to the power-law constitutive equation.

Mode	η	λ	ε	ξ	η_r
1	0.5052e-05	0.1000e-01	0.1197e-01	0.1915	0.6911e-01
2	0.1220e+02	0.2154	0.5354	0.5158e-04	0.6911e-01
3	0.5764e+02	0.4642e+01	0.9358e-02	0.9282	0.6911e-01
4	0.1283e+03	0.1000e+03	0.9325e-02	0.9260	0.6911e-01

Table 4-2. Curve fitting results for the parameters of 4-mode PTT model.

We used these parameters to run flow simulations for both the PTT model and the power-law model. The results are shown in Figure 4-6 as spreading length vs. time. To validate the power-law model results, we also plotted the results using our previous power-law simulation [35], and the new POLYFLOW power-law model result was plotted in red curve. The results show there is only a slight difference between the two power-law model simulations, which differ in their mathematical model. The difference may be because the POLYFLOW simulation of the power-law fluid flow solved the full Navier-Stokes equations and used the ALE method to track the free surface, while in our previous power-law code, we used a lubrication approach to neglect the inertial terms of the Navier-Stokes equations and the free surface was calculated using the thin film equation [35].

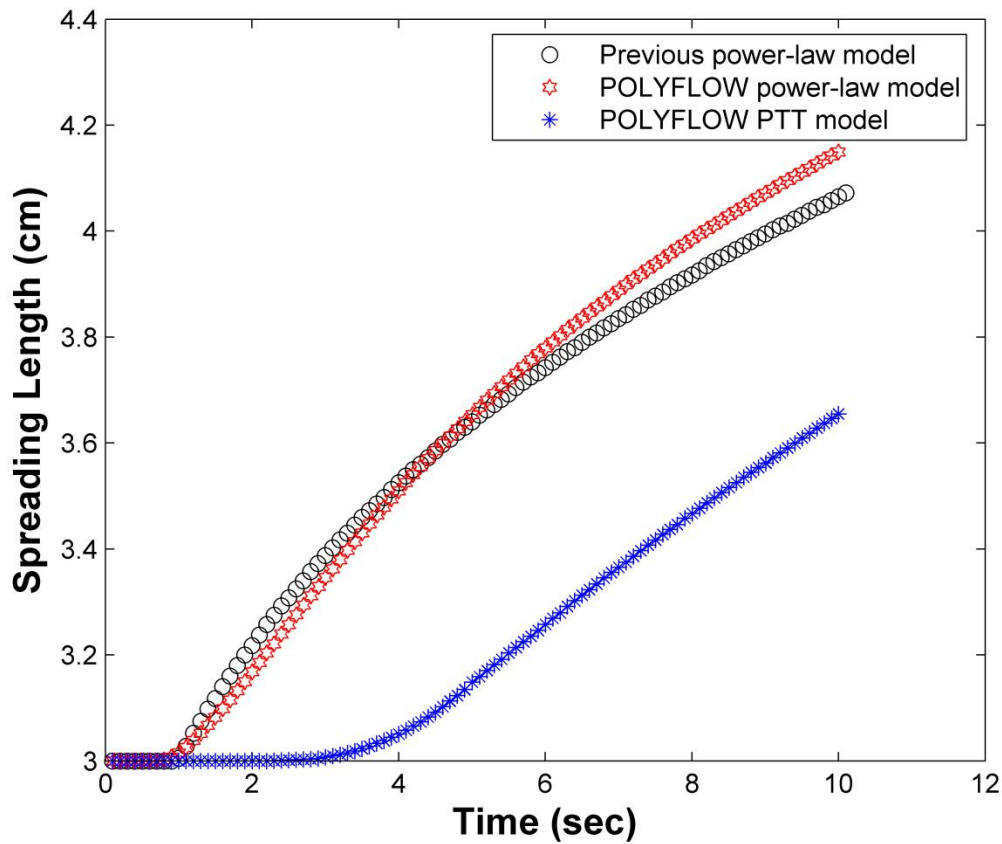


Figure 4-6. Results of microbicide gel spreading for different models. The blue curve indicates the spreading speed from the PTT model simulation, while the red and black curves are the results from power-law models.

Figure 4-6 also shows that compared to the power-law results, we can conclude that in the PTT model, the microbicide gel spreads slower, especially at the beginning of the flow. A way to explain the differences in flow using power-law vs. PTT is to use an energy analysis. Gravitational potential energy is transferred to kinetic energy during the gravity-driven flow process. In the PTT model, a portion of the total energy is stored in the fluid due to the elastic effect, while in the power-law model, there is no energy stored. Assuming the two models have similar amounts of energy dissipated as heat, since they have similar viscosity curves, the

power-law model transferred more energy to kinetic energy; therefore, it spreads faster.

The observations from our previous numerical and experimental studies using the power-law model [64] are consistent with this study because the PTT model indicates the elastic effect of the fluid may slow the initial flow as observed experiments. This indicates that the elastic effect of a microbicide gel is important, and a more accurate constitutive model than power-law model, such as the PTT model, should be used in simulating the microbicide spreading.

4.4. Epithelial squeezing flow model

4.4.1. Problem and methods

Both gravitational and squeezing forces are important in the microbicide delivery process. In this section, the goal was to model the spreading of the microbicide gel on the epithelial surface under the squeezing force of vaginal tissue. As mentioned in the introduction and shown in Figure 4-1 (a) and (b), we focus on the fluid and tissue interaction during the delivery process of microbicide gels.

Figure 4-7 shows the geometry and boundary condition used to approximate the application of a gel to a human vagina. During the insertion process, the epithelial tissue is deformed and the fluid-tissue interface needs to be recalculated. Zero displacement is imposed on the other three boundaries of the epithelial tissue. Steady-state and isothermal conditions are assumed for the system. We use the PTT fluid model to describe the flow in the fluid region.

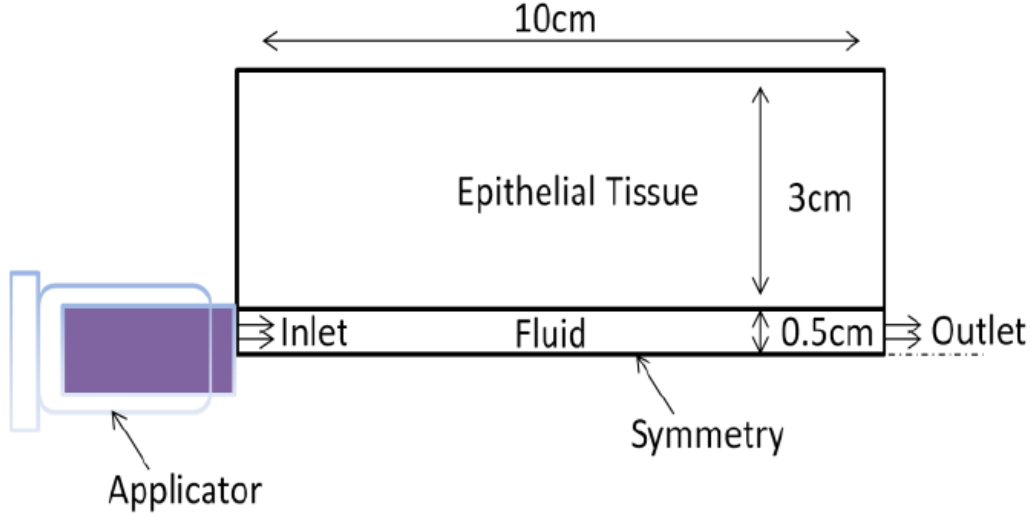


Figure 4-7. Geometry and boundary condition of the model describing insertion of a microbicide gel (“fluid” in diagram) between the vaginal epithelial tissue.

We use a fluid-structure interaction (FSI) model to take into account the elasticity of a solid region (the vaginal tissue surrounding the vaginal lumen) coupled with the adjacent flow problem (the microbicide gel in the vaginal lumen). With body force f , the motion equation for displacement in the solid region is,

$$\nabla \cdot \sigma + f = 0$$

The transient term is neglected, since we assume steady-state flow. For a small deformation, the stress tensor is defined by the following constitutive equation:

$$\sigma = \frac{E}{1 + \nu} \left(\frac{\nu}{1 - 2\nu} \text{tr}(\epsilon) I + \epsilon \right)$$

where E is Young’s modulus, ν is Poisson’s ratio, and ϵ is the strain tensor, defined by displacement d ,

$$\boldsymbol{\varepsilon} = \frac{1}{2} ((\nabla d)^T + \nabla d)$$

Although vaginal epithelial tissue may exhibit viscoelastic behavior, we used the pure elastic constitutive model as the first step of the study to approximate the tissue deformation. Additionally, due to the capability of the POLYFLOW software, it is not possible to simulate the viscoelastic deformation in the solid region using the FSI model. For tissue elasticity, we chose a range based on published literature estimating tissue elasticity under compression in [78]. In that study, the authors found the average values for tissue elasticity for the anterior and posterior compartments for normal conditions were 7.4 ± 4.3 kPa, 6.2 ± 3.1 kPa, and 1.8 ± 0.7 kPa and 1.8 ± 0.5 kPa for prolapsed ones.

These formulations were coupled with the momentum conservation equation and mass conservation equation to solve the complex problem with FSI and viscoelasticity included. The same numerical methods were used for the fluid region. The only difference is that an elastic based remeshing method is used instead of Lagrangian remeshing method of Section 4.3.

4.4.2. Results and discussion

A series of parametric analyses were performed to study the influence of the tissue elasticity and the elastic effect of the gel on tissue deformation and the velocity profile of the flow. The elastic effect of the gel is characterized by the dimensionless Deborah number, which is defined as,

$$De = \lambda \dot{\gamma}$$

where $\dot{\gamma}$ is the characteristic shear rate, given by,

$$\dot{\gamma} = \frac{u}{h}, \quad u = \frac{Q}{2Lh}$$

and where u is the average velocity, and L and h are the width and thickness of the flow region, and Q is the volumetric flow rate.

The effect of tissue elasticity is examined first. According to Ref. [78], we chose $E=5$ kPa for the majority of the simulations, and chose $E=0.5$ kPa for the comparison purposes. In Figure 4-8, the results are shown for two cases, with all other parameters held constant. The plots show both the tissue shape (as contours of displacement) and the fluid velocity. The displacement of the tissue increased for the less stiff (lower E) tissue. In the flow region, the velocity increased with increasing stiffness (higher E).

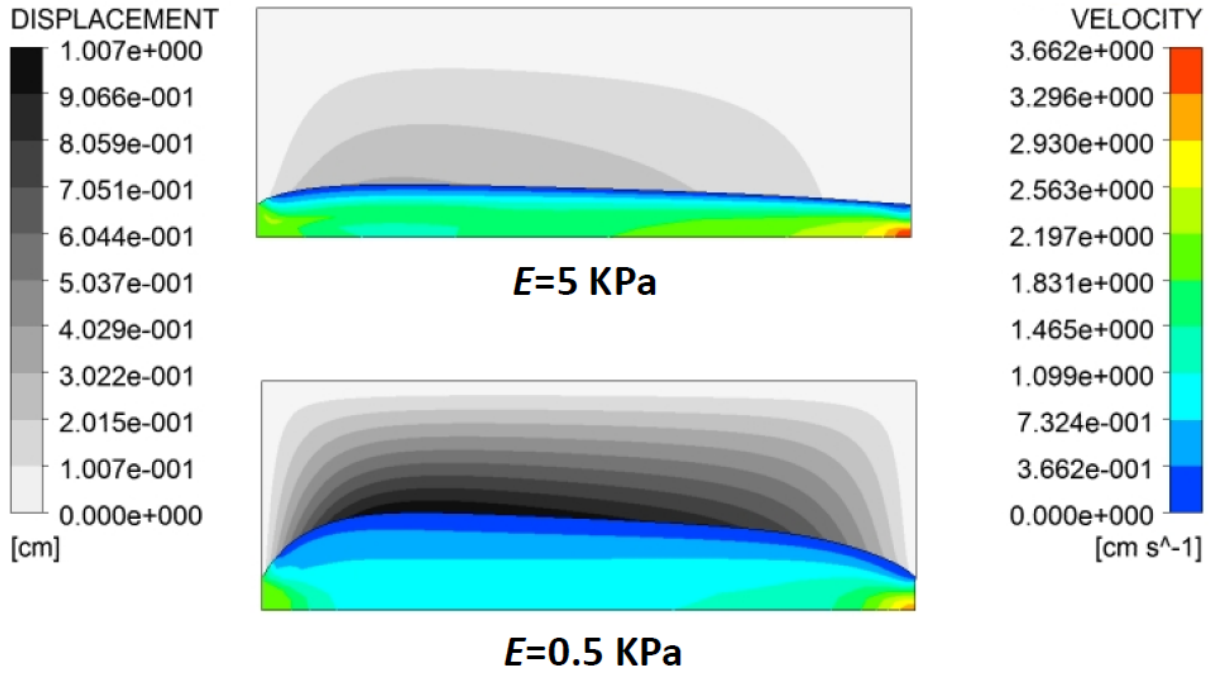


Figure 4-8. Contours of displacement in the tissue region (left contour map) and velocity in the fluid region (right contour map) for different tissue elasticities, with constant $E=5$ kPa (top) and $E=0.5$ kPa (bottom), with constant $Q=1$ cm³/sec, $\nu=0.25$, $\eta=200$ P, $\eta_r=0.2$, $\lambda=1$ s, $\varepsilon=0.01$, and $\xi=0.01$.

Poisson's ratio is also an important material parameter of human tissue. We chose 0.495 as a characteristic value for the tissue region, according to typical values for biological soft tissues (e.g. Ref. [79]), and 0.25 as a reference value for the comparison purposes. Figure 4-9 shows results for the two Poisson's ratios. Displacement of the tissue decreased for a higher Poisson's ratio. This is because the deformation is absorbed more in the other direction for higher Poisson's ratio.

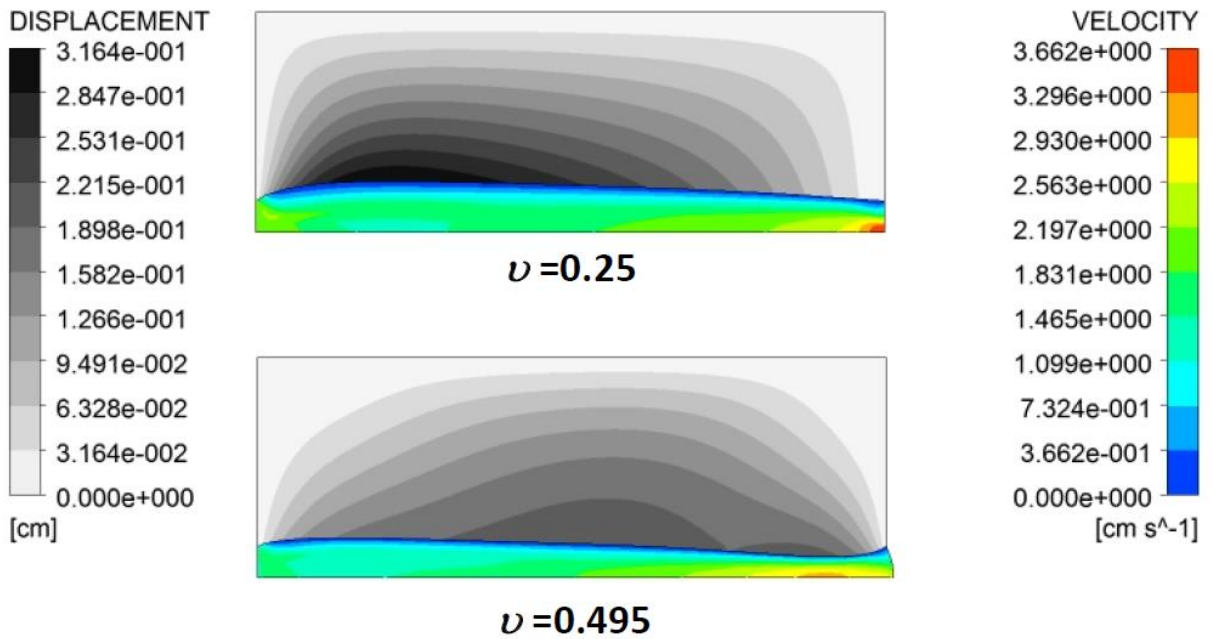


Figure 4-9. Contours of displacement in the tissue region and velocity in the fluid region for two Poisson's ratios, with constant $Q=1$ cm³/sec, $E=5$ kPa, $\eta=200$ P, $\eta_r=0.2$, $\lambda=1$ s, $\varepsilon=0.01$, and $\xi=0.01$.

Figure 4-10 shows how inflow rate influences the results. The results are as expected: as inflow rate increased, both the displacement of the tissue and the velocity of the flow increased. Compared to the tissue elasticity results in Figure 4-8, the impact of the tissue elasticity on the deformation is more dramatic than the inflow rate for these particular parametric settings.

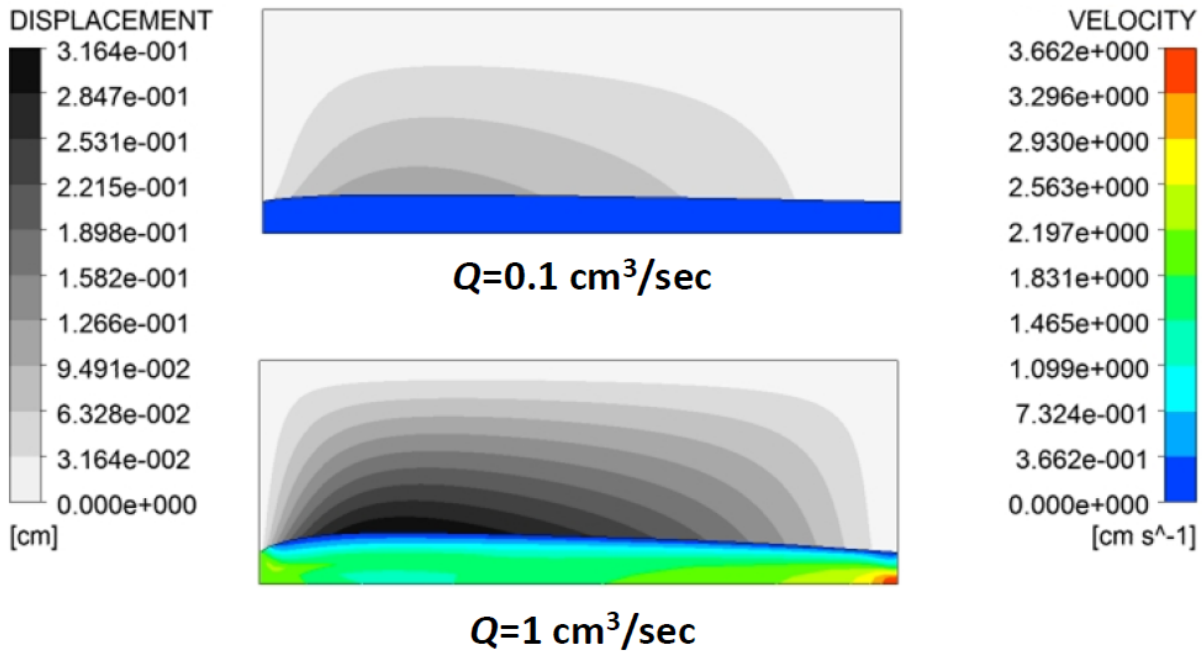


Figure 4-10. Contours of displacement in the tissue region and velocity in the fluid region for two inflow rates, with constant $E=5 \text{ kPa}$, $\nu=0.25$, $\eta=200 \text{ P}$, $\eta_r=0.2$, $\lambda=1 \text{ s}$, $\varepsilon=0.01$, and $\xi=0.01$.

It's also interesting to see how the gel's viscoelasticity affects tissue deformation of the tissue, and thus the distribution of the fluid over the tissue. Figure 4-11 shows displacement at the fluid-solid interface vs. the x -direction position for three values of Deborah numbers (obtained by changing λ). Displacement of the tissue decreases with increasing Deborah number. A higher

Deborah number indicates that the fluid more elastic, i.e. it has a higher elastic component than a fluid with a lower Deborah number. This result can be interpreted as the more elastic gel deforms surrounding tissue less than the less elastic gel. This is because for the same inflow rate and the same systematic energy, more elastic fluid can store more and dissipate less energy. Therefore, less work is done on pushing the tissue wall. The differences seen in Figure 4-11 indicate that the elasticity of the gel will influence the evenness of the gel distribution of the tissue during application.

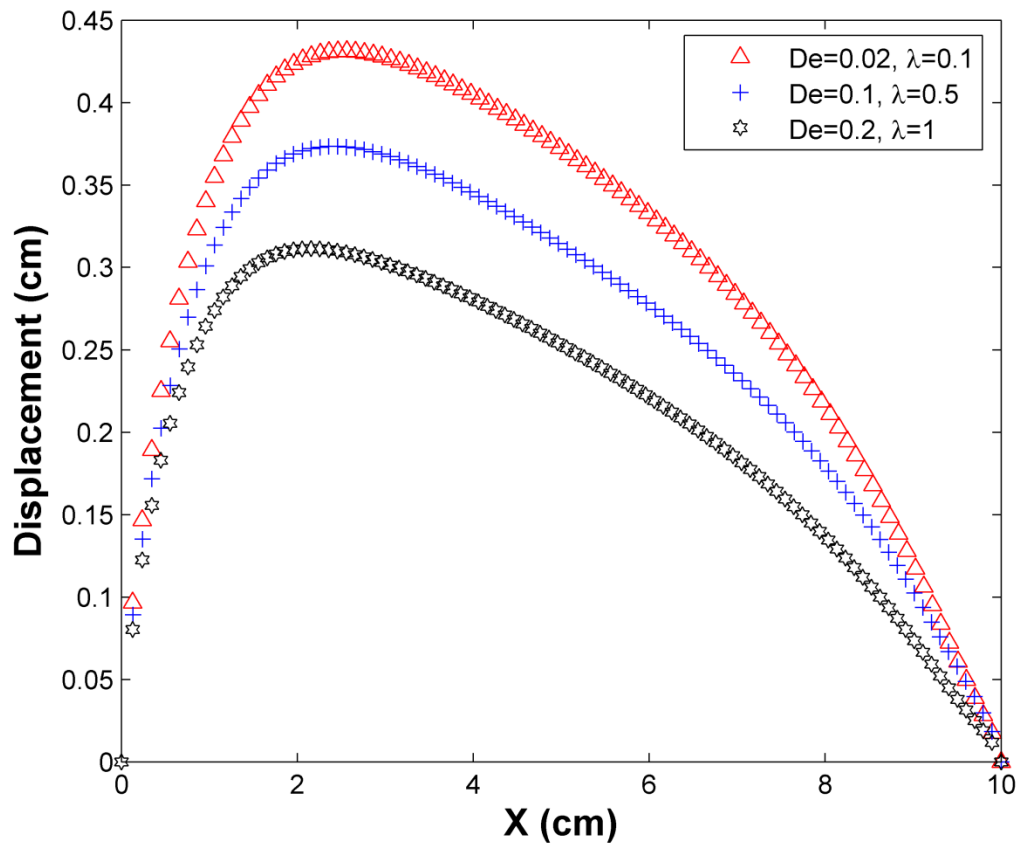


Figure 4-11. Plot of displacement in the tissue region for different Deborah numbers and constant $Q=1 \text{ cm}^3/\text{s}$, $E=5 \text{ kPa}$, $\nu=0.25$, $\eta=200 \text{ P}$, $\eta_r=0.2$, $\varepsilon=0.01$, and $\xi=0.01$.

4.5. Summary

Two mathematical models were developed in this chapter to investigate the viscoelastic effect of microbicide gels during the drug delivery process. In the gravity-driven flow model, several parametric studies were carried out to show how the PTT parameters influence the spreading speed of thin film flow. We also compared the PTT flow simulation to the simple shear-thinning power-law simulation result using rheological data as input. The simulations showed a slower spreading speed with the PTT fluid than the power-law fluid, because more energy is stored in the PTT fluid due to the elastic behavior. These results may explain previous experimental observations that power-law simulations do not represent the early slow flow observed in experiments.

In the squeezing flow model, we examined the displacement of the epithelial tissue under different parametric settings. We found Simulations showed that less stiff tissue and fluids with lower Deborah number can cause more epithelial deformation. The shape of the epithelial deformation upon gel insertion determined the distribution of the gel over the epithelium. These results provide insights into how to design the optimal properties of microbicide gels. First, differences in tissue elasticity may result in different flow characteristics and different gel coverage. Thus, different women with different tissue elasticities should have options for specifically designed gels. Second, according to the study of the inflow rate, speed of microbicide gel insertion can be optimized for different women with different tissue elasticities and different designed gels. Such information could lead to improved labelling instructions for

use to achieve a more even distribution of the gel upon insertion. Moreover, this study is a good supplement to our previous elastic boundary spreading study [25, 75]. The result of this study can be a more practical initial condition of the later spreading process, rather than using an arbitrary initial shape of the gel after insertion.

5. CONCLUSIONS AND FUTURE WORK

5.1. General conclusions

In summary, this PhD dissertation is intended to contribute to the overall goal of optimizing a polymer solution for optimal flow performance and coverage on epithelial surfaces. This work was focused on mathematical modeling and numerical simulation. The objective of this dissertation was to examine the effect of a fluid's properties (e.g., surface tension and rheology) on the fluid's spreading and coating characteristics (e.g., fingering instabilities and spreading speed). A few mathematical models were developed towards this goal, including 2D, LSA, 3D power-law models and a 2D PTT model for the gravity-driven flow and FSI model for the squeezing flow. These mathematical tools can be used to:

- Identifying the surface tension effect on microbicide coating flow
- Examining how a fluid's properties affect the fingering instabilities and ways to suppress the fingering coating in order to avoid uncovered “bare” spots
- Identifying the viscoelastic effect of microbicide gels on both gravity-driven flow and squeezing flow
- Evaluating the flow behavior of the microbicide under the epithelial tissue deformation

The results from these studies are very useful for microbicide development. First, these studies can be used to specify target properties for optimal flow behavior. For example, we should design the vehicle for less shear-thinning to avoid the occurrence of the fingering

instabilities. Another research component of our lab, computational molecular design, can be incorporated here to achieve this goal. For example, the structure of the drug delivery can be designed to achieve those target properties. Additionally, the studies can be used to specify to users how to improve the use of the microbicide. For example, posture during microbicide gel application can be optimized, due to our parametric study on the inclination angle in Chapter 2. Such information could lead to improved labelling instructions for use. In a similar example, different women with different tissue elasticities can choose the specifically designed gels, according to our simulation results on the tissue elasticity in Chapter 4.

5.2. Limitations and future work

There are some limitations to this study, which can guide and improve our future studies.

Effect of contact angle on the surface tension models

I assumed complete wetting in all the models using thin film lubrication approach. However, we expect the contact angle can also affect the microbicide coating. It is interesting to know how the different contact angles can influence the spreading speed of the fingering instabilities. Because we added surface tension through the pressure term of the conservation of momentum equation, it is challenging to incorporate the contact angle, especially the dynamic contact angle. According to the published work in literature, the majority of the studies using lubrication approximation assumed a complete wetting substrate. To incorporate contact angle to our

mathematical models in future, I suggest to introduce more approximations for the fluid-solid contact interaction at the contact line. A similar approach can be found in the droplet studies, e.g., [37].

Limitation of power-law model

As we addressed in Chapter 2 and 3, the power-law rheological model is a simple constitutive model to describe the shear-thinning behavior of the microbicide gels. However, it's not very accurate at the low shear rate region. Others in our research group have improved the current gravity-driven flow models using better constitutive models. Kheyfets developed an Ellis model to address the inaccuracy of the power-law model at the low shear rate [31]. Anwar incorporated yield stress using Herschel–Bulkley model [75]. In the future, we want to keep improving out constitutive models using our own code. As discussed in Chapter 4, it is challenging to use a complicated viscoelastic model, e.g., PTT model using the current lubrication approach, which is our ultimate goal. But it's achievable to incorporate simpler viscoelastic models into our current models in the near future.

Limitation of using a commercial CFD package.

As mentioned in Chapter 4, due to the complexity of the problems, we decided to use CFD software as the solver to simulate the viscoelastic behavior of the microbicide and the FSI squeezing flow. This provides an easy way to solve a broad scope of complicated fluid problems. It reduced the numerical manipulation and let us focus on the physical modeling. However, we had

less control and freedom due to the limitations of the software package. For example, it's interesting to know how the viscoelastic parameters affect the fingering instabilities. We developed a 2D PTT model using POLYFLOW, but due to the capability of the package, it's hard to carry out a linear stability analysis for the fingering instabilities, similarly to what we presented in Chapter 3. As I just mentioned, we are in process of improving our own simulation codes. Understanding how these CFD programs work is helpful in developing our own codes. The CFD packages can also be used to verify the correctness of the codes we are going to develop in future.

Non-dimensional study of the gravity-driven flow of viscoelastic fluids

As discussed in Chapter 4, the Deborah number is a useful dimensionless group for interpreting viscoelastic fluid flow. It quantifies how important the elastic behavior is compared to viscous behavior. However it's not appropriate to use it in our current gravity-driven flow model, which was pointed out by Dealy [76]. We carried out dimensional studies and compared our PTT model to the previous power-law model. The results can reflect the elastic effect of the microbicide gels in the gravity-driven flow as we discussed in Chapter 4. However, we couldn't isolate the elastic effect well from the PTT model itself. Future work will involve more approximations and developing our own code using the non-dimensional equations.

Combination of gravity-driven flow model and the squeezing flow model

Gravity-driven flow and squeezing flow models are independently studied to simplify the problem. By using the CFD packages, it's possible to combine the two models into one to see the combined effect of gravity and squeezing forces. Additionally, in the future, we can model a more realistic vaginal cavity geometry to investigate the effect of the vaginal structure.

Incorporations in the research group

As a parallel research component, this study can be incorporated with other research topics in our research group. For example, more realistic tissue elasticity and/or viscoelasticity can be obtained from Mark Pacey's experimental apparatus, developed to measure the elasticity of vaginal tissue *in vivo* [80]. The ultimate goal of this study is to obtain the molecular structure-properties-function relationship for the optimal design of the microbicides. A preliminary attempt in this direction has been done by Anwar from our research group [75]. In his study, he was able to identify a set of target properties, e.g., tissue elasticity and yield stress of the microbicide gels, for the target flow behavior, e.g., maximal retention and target coating length. Similarly, the numerical results presented in this dissertation are helpful for another branch of the lab research, computational molecular design carried by Thora Whitmore [77]. However, the parametric range in the current study is set for the purpose of theoretical analysis. To better serve the molecular design, more realistic values are needed to find the target values.

5.3. Summary

The analysis in this dissertation presented several new mathematical models to simulate the spreading of microbicide gels during the drug delivery process. Power-law and PTT constitutive models were used for the non-Newtonian behavior of the microbicide gels. Both gravity-driven flow and squeezing flow models were studied for the first time. This dissertation provided insight into how to design microbicide gels with optimal properties for target performance.

The use of the mathematical models presented in this dissertation is not limited to the microbicide development. Other thin film coating flow applications can also benefit from this study, e.g., paints, contact lens manufacture and microchip fabrication, etc.

6. APPENDIX

Appendix A: Sensitivity study of precursor thickness

Many previous works have studied the influence of the precursor thickness. Both numerical [16, 50] and experimental [65] studies have indicated that increasing the thickness of the precursor can decrease the size of the capillary ridge and suppress the contact line instability.

Figure A.1 shows the comparison between different precursors: $b=0.001\text{cm}$ (black solid), $b=0.01\text{cm}$ (blue dotted) and $b=0.05\text{cm}$ (red dashed).

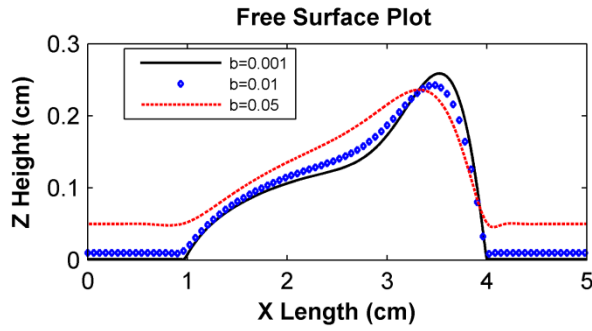


Figure A.1. (Color online) Comparison of the free surfaces between the results for different precursor thicknesses: $b=0.001\text{ cm}$ (black solid), $b=0.01\text{ cm}$ (blue dotted) and $b=0.05\text{ cm}$ (red dashed). (Parameters used in the simulation: $m=100\text{ Ps}^{n-1}$, $n=0.8$, $\alpha=60^\circ$, $\gamma=70\text{ dyn/cm}$, $H=0.3\text{ cm}$)

We can see the capillary ridge height goes down when we increase the precursor thickness b .

This agrees with the previous literature.

Appendix B: Similarity solution for power-law fluids

Far behind the front region where surface tension dominates, the height profile of the gel can be described by a similarity solution. For Newtonian fluids, a similarity solution was obtained by Huppert [58],

$$h(x,t) = \sqrt{\frac{\mu x}{\rho g \sin \alpha t}}.$$

This expression indicates that the thickness of the free surface decreases on the scale of $H_N \sim t^{-1/3}$ at a relatively long time after initial condition, and it is independent of the initial condition.

Following the method outlined in [58], we can obtain the similarity solution for the power-law fluid as

$$h(x,t) = \left(\frac{m}{\rho g \sin \alpha} \right)^{\frac{1}{n+1}} \left(\frac{x}{t} \right)^{\frac{n}{n+1}}. \quad (\text{B.1})$$

By setting $n=1$, this expression reduced to Huppert's Newtonian similarity solution.

Assuming a zero surface tension in our model ($\gamma=0$), we compared the result from our numerical model to this power-law similarity solution. We compared for both Newtonian fluids (Figure B.1) and shear-thinning fluids (Figure B.2) using two different initial conditions $H=0.2\text{cm}$ and $H=0.45\text{cm}$. As shown in the figures, all four cases agree with the similarity solution. We can see the gels start from different initial conditions, and after a relatively long spreading time (110 s), the free surfaces approach the similarity solution profile. Although the Newtonian gels flow faster than the shear-thinning gels for these settings, the similarity solution

very accurately describes the difference. Thus, through this study, we verified our numerical model using the similarity solution.

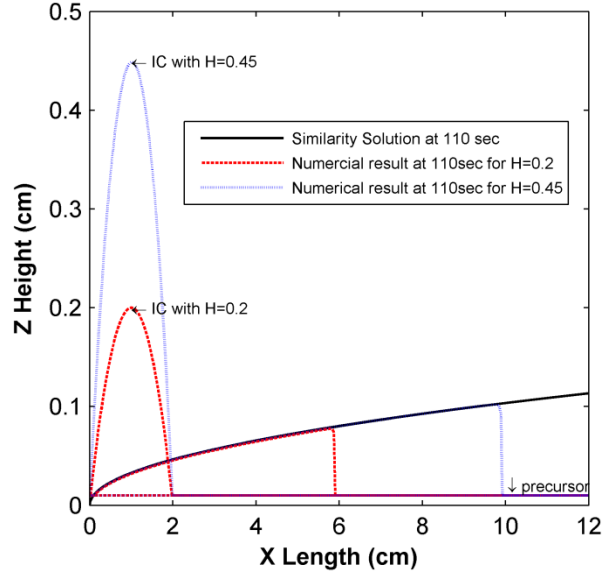


Figure B.1. Comparison of the free surface spreading of the similarity solution (black solid) and the numerical model at 110 s for Newtonian fluids. Two different initial conditions: $H=0.2$ cm (red dashed) and $H=0.45$ cm (blue dotted). Parameters: $m= 100 \text{ Ps}^{n-1}$, $n=1$, $\alpha=60^\circ$ and $\gamma=0 \text{ dyn/cm}$.

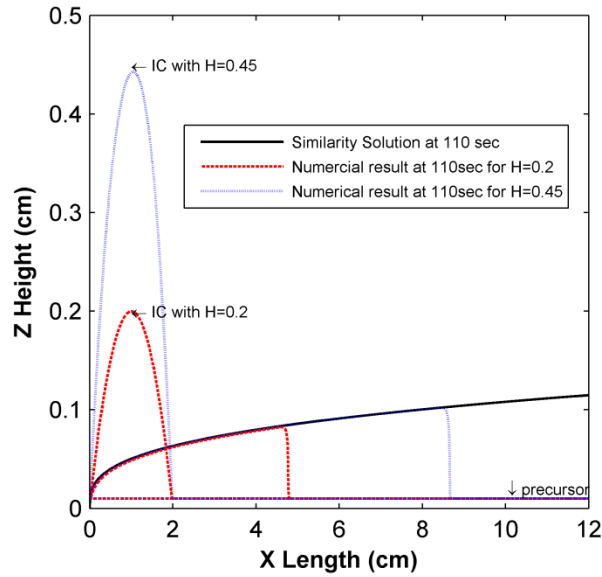


Figure B.2. Comparison of the free surfaces spreading of the similarity solution (black solid) and the numerical model at 110 s for shear-thinning fluids. Two different initial conditions: $H=0.2$ cm

(red dashed) and $H=0.45\text{cm}$ (blue dotted). Parameters: $m=100 \text{ Ps}^{n-1}$, $n=0.5$, $\alpha=60^\circ$ and $\gamma=0 \text{ dyn/cm}$.

Appendix C: Traveling wave solution for power-law fluids

By assuming a simplified constant flux flow, we compared the result from our numerical model to the traveling wave solution. We used the constant flux boundary conditions $x \rightarrow -\infty, h \rightarrow 1$ and $x \rightarrow \infty, h \rightarrow b$ for Eq. (3) in Chapter 2 (where b is thickness of the precursor). This boundary condition leads to a traveling wave solution $h(x, t)$ for Eq. (3). If we define $h(x, t) = h_0(x^*)$, where $x^* = x - Ut$, and U is the velocity of the traveling wave, then the function $h_0(x^*)$ must satisfy

$$-Uh_0 + m^{-\frac{1}{n}} \frac{n}{2n+1} \left\{ h_0^{\frac{1}{n}+2} [\rho g (\sin \alpha - \cos \alpha h_{0x^*}) + \gamma h_{0x^*} x^* x^*]^{\frac{1}{n}-1} [\rho g (\sin \alpha - \cos \alpha h_{0x^*}) + \gamma h_{0x^*} x^* x^*] \right\} = f$$

Refer to [15] for more details about traveling wave solution of the thin film equation.

Applying the two boundary conditions, $x^* \rightarrow -\infty, h_0 \rightarrow 1$ and $x^* \rightarrow \infty, h_0 \rightarrow b$, we can get

$$U = m^{-\frac{1}{n}} \frac{n}{2n+1} (\rho g \sin \alpha)^{\frac{1}{n}} \left(\frac{1 - b^{\frac{1}{n}+2}}{1 - b} \right). \quad (\text{C.1})$$

$$f = m^{-\frac{1}{n}} \frac{n}{2n+1} (\rho g \sin \alpha)^{\frac{1}{n}} \left(\frac{-b + b^{\frac{1}{n}+2}}{1 - b} \right).$$

Using the 2D numerical model developed in this study, we can compare the result of our numerical solution to the traveling wave solution. We used a smooth step function as the initial condition,

$$h(x) = \frac{1}{b} \frac{1}{1 + \exp(-4(-(x-10)))} \quad \begin{matrix} 0 \leq x \leq 10 \\ 10 < x \leq 40 \end{matrix},$$

in our 2D model. Figure C.1 shows the numerical simulation results plotted over 10 seconds.

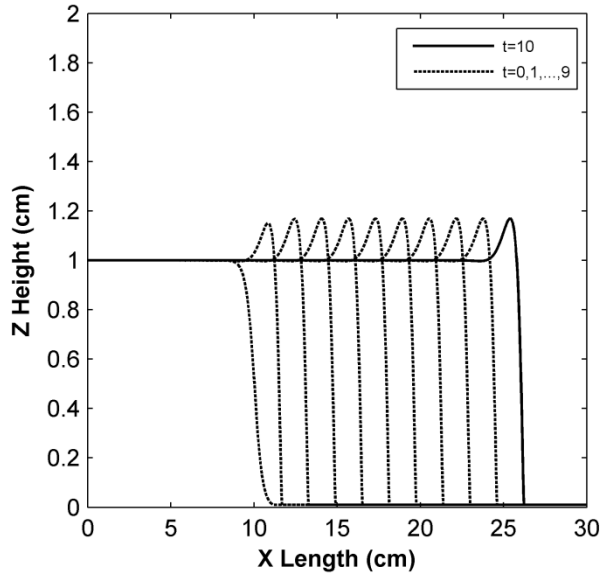


Figure C.1. Evolution of free surface using constant flux in the numerical simulation, total time=10s, sampling=1s. (Parameters used in the simulation: $m=200\text{Ps}^{n-1}$, $n=0.9$, $\alpha=60^\circ$, $\gamma=40\text{dyn/cm}$, $b=0.01\text{cm}$)

The velocity calculated in the simulation ($U=1.6200$) had a great agreement with the traveling wave solution ($U=1.6178$) (Eq. (C.1)).

Appendix D: Non-dimensional study for 2D power-law fluids

Following the non-dimensionlization in [16], the dimensionless variables can be introduced

using the characteristic film thickness H_N , film length L , time T and velocity U :

$$h = \frac{h}{H_N},$$

$$x = \frac{x}{L},$$

$$\tilde{t} = \frac{t}{T}.$$

Here, H_N is the thickness of the profile described in the power-law similarity solution, as introduced in Appendix B. $L = H_N / (C_a)^{1/3}$, where $C_a = \mu_0 U / \gamma$ is the power-law capillary number and $\mu_0 = m(U/H_N)^{n-1}$ is the characteristic viscosity.

Because the flow field away from the front determines the characteristic velocity, we can estimate the characteristic time scale, T , using the power-law similarity solution (Eq. (B.1)),

$$T = (H_N)^{-\left(\frac{1}{n}+1\right)} \left(\frac{m}{\rho g \sin \alpha} \right)^{\frac{1}{n}} L.$$

so that the characteristic velocity $U \sim L/T$, and the capillary number can be approximated as

$$C_a = \frac{\mu_0 U}{\gamma} \approx \frac{\rho g \sin \alpha H_N^2}{\gamma}.$$

Substituting these dimensionless variables as well as the capillary number C_a into Eq. (3),

we get the non-dimensional evolution equation:

$$\frac{\partial h}{\partial t} + \frac{n}{2n+1} \frac{\partial}{\partial x} \left\{ h^{\frac{1}{n}+2} \left| 1 - \cot \alpha C_a^{\frac{1}{3}} \frac{\partial h}{\partial x} + \frac{\partial^3 h}{\partial x^3} \right|^{\frac{1}{n}-1} \left(1 - \cot \alpha C_a^{\frac{1}{3}} \frac{\partial h}{\partial x} + \frac{\partial^3 h}{\partial x^3} \right) \right\} = 0.$$

(D.1)

If we define $D = \cot \alpha C_a^{1/3}$, which is an important quantity indicated in [16], then Eq. (D1)

becomes only dependent on two dimensionless parameters: D and shear-thinning index n .

To directly compare to the literature, Eq. (D.1) was solved with the constant flux condition as introduced in Appendix C. The result is similar in shape to the result shown in Figure C.1. The dependence of the dimensionless maximum height of the flow profiles on D and n is shown in

Figure D.1.

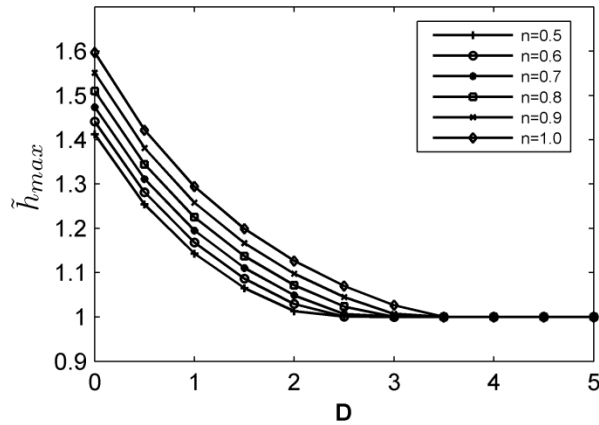


Figure D.1. Dimensionless maximum height of the flow profiles as a function of D for different values of shear-thinning index n .

Because we used a constant flux setup, the capillary ridge height can be simply calculated by $h_{cr} = h_{\max} - 1$. As we can see from Figure D.1, for both Newtonian fluids ($n=1$) and non-Newtonian fluids ($n<1$), the capillary ridge height reduces as D increases. This result agrees with the parametric study of D for Newtonian fluids in [16]. Moreover, it indicates that the more shear-thinning the fluid is, the smaller capillary ridge occurs, as also found in our dimensional study.

Appendix E. Fluorescence Imaging Measurement

Henry M. Clever and I worked together on this study, with the guidance of Dr. Sarah L. Kieweg and contributions from Dr. Carey K. Johnson (Chemistry, KU). I first identified the experimental approach and ideas, and built the initial apparatus. Henry worked with me and Dr. Kieweg on the details of the experimental approach, and to modify the experiment for images. I also supervised Henry on the development of MATLAB code to process and analyze the images. This work may be submitted for publication. Here, I summarize the overall work, and identify the challenges with these experiments.

The motivation of this study was to develop an experiment to observe and compare the contact line fingering instabilities we discussed in Chapter 2-3. After I developed the original ramp apparatus, we were able to observe various contact line fingering patterns along with the

capillary ridge at the front under different flow conditions, as shown in Figure E.1. In order to quantitatively measure the experimental data, e.g., fluid thickness and flow speed, I proposed the idea of developing a fluorescent imaging system using green LED. Henry joined to this project through an undergraduate research program in Dr. Kieweg's laboratory. Henry and I worked together on the experiment design, such as selecting the fluorescent dyes, building the illumination and filtering system, developing the image processing algorithm, etc. Under my mentorship, Henry developed the calibration and normalizing methods, and carried out most of the experiments independently.

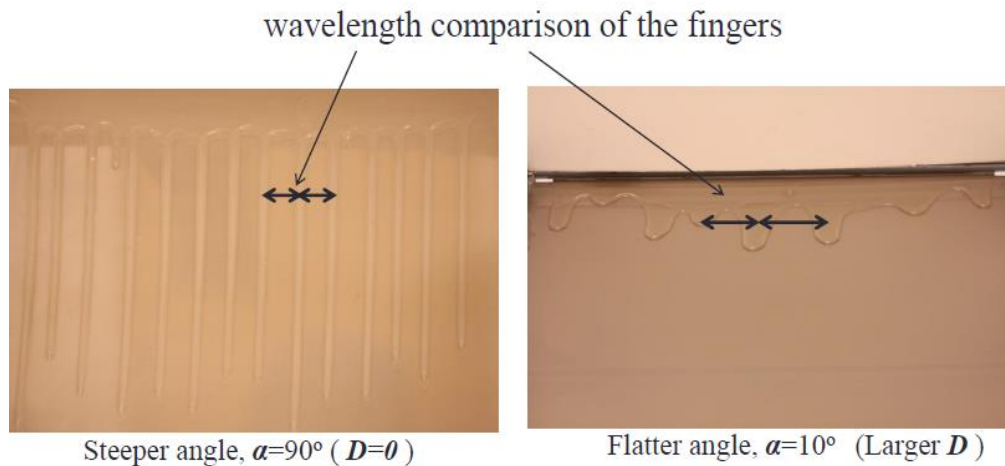


Figure E.1. Example of the fingering patterns observed using the original ramp apparatus.

In this study, we developed an imaging system with fluorescent dye to image fluids as they flow down an incline. Instead of using the currently widely used laser-induced fluorescence (LIF) method, we tried to create a much more inexpensive system using LEDs as a form of illumination. We chose green LEDs to excite the dye and captured the imaging of the light

emitted by the dye using a digital camera. The light/pixel intensity of the image can be converted to the fluid depth using previously published formulations. The flow area we try to measure in this study is relatively large compared to the studies in literature. To get evenly distributed illumination of the target surface area, we need to conquer two challenges, the first being the orientation of LED lighting around the surface of fluid. Next, camera images are subject to vignetting, a phenomenon that and occurs due to lens aperture size. We developed a normalizing method to solve these issues.

By using the imaging system we developed in this study, we can measure the depth of fluid in a large target area. Additionally, the changing pattern and moving speed of the contact line can also be obtained and calculated. Therefore, in future, we can further verify the results we obtained in Chapter 2 and 3. Two examples of the applications are shown in Figure E.2 and Figure E.3.

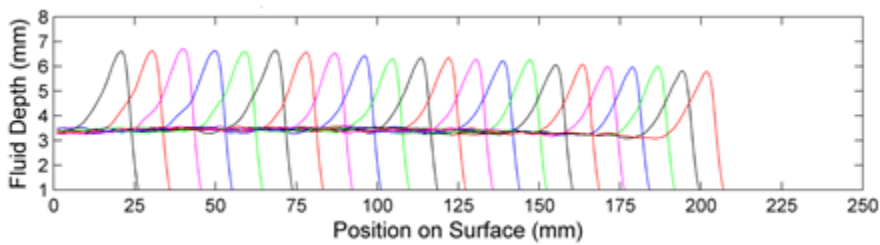


Figure E.2. Cross depth plot showing the evolution of free surface at the front of a finger, which can be used to compare the results in Chapters 2 and 3, e.g., Figure 2-2 and Figure C.1.

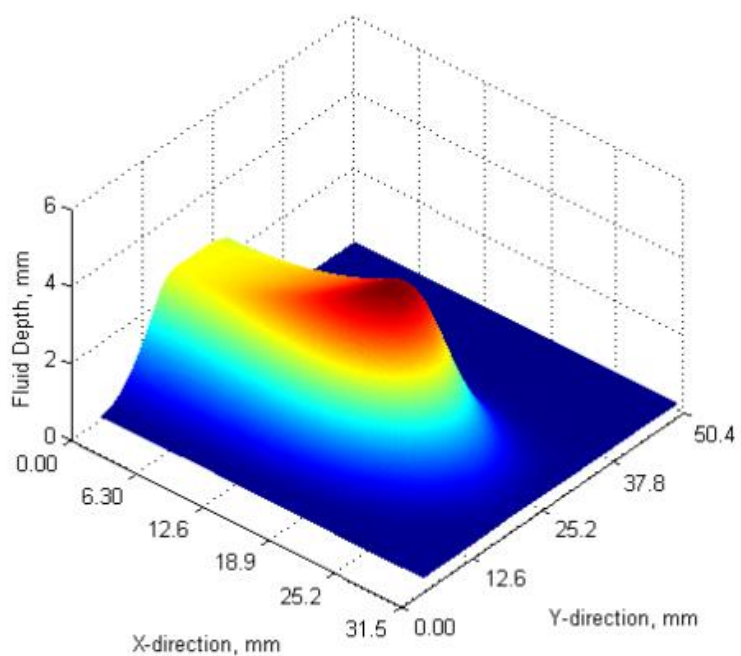


Figure E.3. 3D plot of a single propagating finger obtained and calculated using fluorescence imaging.

There are a few challenges for this study. The experimental setting requires loading the gel in the trough repeatedly. To quantitatively compare the simulations, e.g., power-law model results, we need to use the controlled value of m and n for the comparison purpose, which is impossible when we try to make gels in reality.

7. REFERENCES

- [1] UNAIDS, 2016, "Global AIDS Update."
- [2] WHO, 2009, "Women's Health," World Health Organization, Fact sheet N °334.
- [3] Lederman, M. M., Offord, R. E., and Hartley, O., 2006, "Microbicides and other topical strategies to prevent vaginal transmission of HIV," *Nature Reviews Immunology*, 6(5), pp. 371-382.
- [4] Kieweg, S. L., 2005, "Mechanical analysis of vaginal gels intended for microbicide application," Dissertation, Duke University.
- [5] Karim, Q. A., 2011, "Effectiveness and safety of tenofovir gel, an antiretroviral microbicide, for the prevention of HIV infection in women," *Science*, 333(6042), pp. 524-524.
- [6] Haase, A. T., 2005, "Perils at mucosal front lines for HIV and SIV and their hosts," *Nature Reviews Immunology*, 5(10), pp. 783-792.
- [7] Geonnotti, A. R., and Katz, D. F., 2006, "Dynamics of HIV neutralization by a microbicide formulation layer: Biophysical fundamentals and transport theory," *Biophysical Journal*, 91(6), pp. 2121-2130.
- [8] Veazey, R. S., Klasse, P. J., Schader, S. M., Hu, Q. X., Ketas, T. J., Lu, M., Marx, P. A., Dufour, J., Colonno, R. J., Shattock, R. J., Springer, M. S., and Moore, J. P., 2005, "Protection of macaques from vaginal SHIV challenge by vaginally delivered inhibitors of virus-cell fusion," *Nature*, 438(7064), pp. 99-102.
- [9] Spring, S., 2006, "The Microbicide Development Strategy," A.f.M.D. MDS Working Groups.
- [10] Evans, P. L., Schwartz, L. W., and Roy, R. V., 2000, "A mathematical model for crater defect formation in a drying paint layer," *Journal of Colloid and Interface Science*, 227(1), pp. 191-205.
- [11] Nong, K., and Anderson, D. M., 2010, "Thin film evolution over a thin porous layer: modeling a tear film on a contact lens," *Siam Journal on Applied Mathematics*, 70(7), pp. 2771-2795.
- [12] Pease, L. F., and Russel, W. B., 2003, "Electrostatically induced submicron patterning of thin perfect and leaky dielectric films: A generalized linear stability analysis," *Journal of Chemical Physics*, 118(8), pp. 3790-3803.
- [13] Svendsen, B., Wu, T., Johnk, K., and Hutter, K., 1996, "On the role of mechanical interactions in the steady-state gravity flow of a two-constituent mixture down an inclined plane," *Proceedings of the Royal Society of London Series a-Mathematical Physical and Engineering Sciences*, 452(1948), pp. 1189-1205.
- [14] Partridge, D., and Baines, M. J., 2011, "A moving mesh approach to an ice sheet model," *Computers & Fluids*, 46(1), pp. 381-386.
- [15] Kondic, L., 2003, "Instabilities in gravity driven flow of thin fluid films," *Siam Review*, 45(1), pp. 95-115.

- [16] Bertozzi, A. L., and Brenner, M. P., 1997, "Linear stability and transient growth in driven contact lines," *Physics of Fluids*, 9(3), pp. 530-539.
- [17] Kieweg, S. L., Geonnotti, A. R., and Katz, D. F., 2004, "Gravity-induced coating flows of vaginal gel formulations: In vitro experimental analysis," *Journal of Pharmaceutical Sciences*, 93(12), pp. 2941-2952.
- [18] Kheyfets, V. O., 2011, "Mathematical and experimental analysis of microbicide vaginal gels," Dissertation, University of Kansas.
- [19] Brackbill, J. U., Kothe, D. B., and Zemach, C., 1992, "A continuum method for modeling surface-tension," *Journal of Computational Physics*, 100(2), pp. 335-354.
- [20] de Gennes, P. G., Brochard, W. F., and Quéré D., 2002, "Capillary and Wetting Phenomena -- Drops, Bubbles, Pearls, Waves."
- [21] Flitton, J. C., and King, J. R., 2004, "Surface-tension-driven dewetting of Newtonian and power-law fluids," *Journal of Engineering Mathematics*, 50(2-3), pp. 241-266.
- [22] King, J. R., 2001, "Two generalisations of the thin film equation," *Mathematical and Computer Modelling*, 34(7-8), pp. 737-756.
- [23] Betelu, S. I., and Fontelos, M. A., 2003, "Capillarity driven spreading of power-law fluids," *Applied Mathematics Letters*, 16(8), pp. 1315-1320.
- [24] Kondic, L., and Diez, J., 2001, "Pattern formation in the flow of thin films down an incline: Constant flux configuration," *Physics of Fluids*, 13(11), pp. 3168-3184.
- [25] Karri, S., 2011, "2D thin-film flow of a non-Newtonian fluid between elastic boundaries," master thesis, University of Kansas.
- [26] Borazjani, I., 2013, "Fluid-structure interaction, immersed boundary-finite element method simulations of bio-prosthetic heart valves," *Comput. Meth. Appl. Mech. Eng.*, 257, pp. 103-116.
- [27] Saeid Khalafvand, S., and Han, H.-C., 2015, "Stability of carotid artery under steady-state and pulsatile blood flow: a fluid-structure interaction study," *J. Biomech. Eng.-Trans. ASME*, 137(6).
- [28] Ebrahimi, B., and Hassani, K., 2015, "Modeling of superior mesenteric artery aneurysm using fluid-structure interaction," *J. Mech. Med. Biol.*, 15(1).
- [29] Macosko, C., 1994, "Rheology principles, measurements, and applications," Wiley-VCH, New York, 4th edition.
- [30] Myers, T. G., 2005, "Application of non-Newtonian models to thin film flow," *Phys. Rev. E*, 72(6).
- [31] Kheyfets, V. O., and Kieweg, S. L., 2013, "Gravity-driven thin film flow of an Ellis fluid," *J. Non-Newton. Fluid Mech.*, 202, pp. 88-98.
- [32] Favero, J. L., Secchi, A. R., Cardozo, N. S. M., and Jasak, H., 2010, "Viscoelastic flow analysis using the software OpenFOAM and differential constitutive equations," *J. Non-Newton. Fluid Mech.*, 165(23-24), pp. 1625-1636.
- [33] Lodge, A. S., Renardy, M., and Nohel, J. A., 1985, *Viscoelasticity and rheology*, Academic Press, INC.

- [34]Hu, B., 2008, "The effect of surface tension on the epithelial spreading of non-Newtonian drug delivery vehicles: numerical simulations," Master thesis, University of Kansas.
- [35]Hu, B., and Kieweg, S. L., 2012, "The effect of surface tension on the gravity-driven thin film flow of Newtonian and power-law fluids," *Computers & Fluids*, 64, pp. 83-90.
- [36]Renardy, M., Renardy, Y., and Li, J., 2001, "Numerical simulation of moving contact line problems using a volume-of-fluid method," *Journal of Computational Physics*, 171(1), pp. 243-263.
- [37]Dupont, J. B., and Legendre, D., 2010, "Numerical simulation of static and sliding drop with contact angle hysteresis," *Journal of Computational Physics*, 229(7), pp. 2453-2478.
- [38]Khennner, M., 2004, "Computation of the material indicator function near the contact line (in Tryggvason's method)," *Journal of Computational Physics*, 200(1), pp. 1-7.
- [39]Afkhani, S., and Busmann, M., 2008, "Height functions for applying contact angles to 2D VOF simulations," *International Journal for Numerical Methods in Fluids*, 57(4), pp. 453-472.
- [40]Nikolopoulos, N., Nikas, K. S., and Bergeles, G., 2009, "A numerical investigation of central binary collision of droplets," *Computers & Fluids*, 38(6), pp. 1191-1202.
- [41]Kondic, L., and Diez, J., 2002, "Flow of thin films on patterned surfaces: Controlling the instability," *Phys. Rev. E*, 65(4), p. 4.
- [42]Diez, J. A., and Kondic, L., 2001, "Contact line instabilities of thin liquid films," *Physical Review Letters*, 86(4), pp. 632-635.
- [43]Troian, S. M., Herbolzheimer, E., Safran, S. A., and Joanny, J. F., 1989, "Fingering instabilities of driven spreading films," *Europhysics Letters*, 10(1), pp. 25-30.
- [44]Schwartz, L. W., 1989, "Viscous flows down an inclined plane - instability and finger formation," *Physics of Fluids A: Fluid Dynamics*, 1(3), pp. 443-445.
- [45]Kondic, L., and Diez, J., 2003, "Flow of thin films on patterned surfaces," *Colloid Surf. A-Physicochem. Eng. Asp.*, 214(1-3), pp. 1-11.
- [46]Diez, J. A., and Kondic, L., 2002, "Computing three-dimensional thin film flows including contact lines," *Journal of Computational Physics*, 183(1), pp. 274-306.
- [47]Lin, T. S., and Kondic, L., 2010, "Thin films flowing down inverted substrates: Two dimensional flow," *Physics of Fluids*, 22(5).
- [48]Balmforth, N., Ghadge, S., and Myers, T., 2007, "Surface tension driven fingering of a viscoplastic film," *J. Non-Newton. Fluid Mech.*, 142(1-3), pp. 143-149.
- [49]Gonzalez, A. G., Diez, J., Gomba, J., Gratton, R., and Kondic, L., 2004, "Spreading of a thin two-dimensional strip of fluid on a vertical plane: Experiments and modeling," *Phys. Rev. E*, 70(2).
- [50]Gomba, J. M., Diez, J., Gratton, R., Gonzalez, A. G., and Kondic, L., 2007, "Stability study of a constant-volume thin film flow," *Phys. Rev. E*, 76(4).
- [51]Acheson, D. J., 1990, "Elementary fluid dynamics," Oxford University Press.
- [52]Perazzo, C. A., and Gratton, J., 2003, "Thin film of non-Newtonian fluid on an incline," *Phys. Rev. E*, 67(1).

- [53]Miladinova, S., Lebon, G., and Toshev, E., 2004, "Thin-film flow of a power-law liquid falling down an inclined plate," *J. Non-Newton. Fluid Mech.*, 122(1-3), pp. 69-78.
- [54]Bertozzi, A. L., 1998, "The mathematics of moving contact lines in thin liquid films," *Notices of the AMS(JUNE/JULY)*, pp. 689-697.
- [55]Hu, B., and Kieweg, S. L., 2015, "Contact line instability of gravity-driven flow of power-law fluids," *J. Non-Newton. Fluid Mech.*, 225, pp. 62-69.
- [56]Szeri, A. J., Park, S. C., Verguet, S., Weiss, A., and Katz, D. F., 2008, "A model of transluminal flow of an anti-HIV microbicide vehicle: Combined elastic squeezing and gravitational sliding," *Physics of Fluids*, 20(8).
- [57]Jossic, L., Lefevre, P., de Loubens, C., Magnin, A., and Corre, C., 2009, "The fluid mechanics of shear-thinning tear substitutes," *J. Non-Newton. Fluid Mech.*, 161(1-3), pp. 1-9.
- [58]Huppert, H. E., 1982, "Flow and instability of a viscous current down a slope," *Nature*, 300(5891), pp. 427-429.
- [59]Espin, L., and Kumar, S., 2014, "Forced spreading of films and droplets of colloidal suspensions," *Journal of Fluid Mechanics*, 742, pp. 495-519.
- [60]Espin, L., and Kumar, S., 2014, "Sagging of evaporating droplets of colloidal suspensions on inclined substrates," *Langmuir*, 30(40), pp. 11966-11974.
- [61]Spaid, M. A., and Homsy, G. M., 1996, "Stability of Newtonian and viscoelastic dynamic contact lines," *Physics of Fluids*, 8(2), pp. 460-478.
- [62]Spaid, M. A., and Homsy, G. M., 1997, "Stability of viscoelastic dynamic contact lines: An experimental study," *Physics of Fluids*, 9(4), pp. 823-832.
- [63]Lin, T. S., Kondic, L., and Filippov, A., 2012, "Thin films flowing down inverted substrates: Three-dimensional flow," *Physics of Fluids*, 24(2).
- [64]Kheifets, V. O., and Kieweg, S. L., 2013, "Experimental and numerical models of three-dimensional gravity-driven flow of shear-thinning polymer solutions used in vaginal delivery of microbicides," *J. Biomech. Eng.-Trans. ASME*, 135(6).
- [65]Ye, Y., and Chang, H. C., 1999, "A spectral theory for fingering on a prewetted plane," *Physics of Fluids*, 11(9), pp. 2494-2515.
- [66]Logg, A., and Wells, G. N., 2010, "DOLFIN: Automated finite element computing," *ACM Trans. Math. Softw.*, 37(2).
- [67]Logg, A., Mardal, K.-A., and Wells, G. N., 2012, "Automated solution of differential equations by the finite element method," Springer.
- [68]Khayat, R. E., 2000, "Transient free-surface flow inside thin cavities of viscoelastic fluids," *J. Non-Newton. Fluid Mech.*, 91(1), pp. 15-29.
- [69]Pavlidis, M., Dimakopoulos, Y., and Tsamopoulos, J., 2009, "Fully developed flow of a viscoelastic film down a vertical cylindrical or planar wall," *Rheol. Acta*, 48(9), pp. 1031-1048.
- [70]Khayat, R. E., 2000, "Transient two-dimensional coating flow of a viscoelastic fluid film on a substrate of arbitrary shape," *J. Non-Newton. Fluid Mech.*, 95(2-3), pp. 199-233.
- [71]Favero, J. L., Secchi, A. R., Cardozo, N. S. M., and Jasak, H., 2010, "Viscoelastic fluid

analysis in internal and in free surface flows using the software OpenFOAM," *Computers & Chemical Engineering*, 34(12), pp. 1984-1993.

[72]Olsson, E., Kreiss, G., and Zahedi, S., 2007, "A conservative level set method for two phase flow II," *Journal of Computational Physics*, 225(1), pp. 785-807.

[73]Ganvir, V., Lele, A., Thaokar, R., and Gautham, B. P., 2007, "Simulation of viscoelastic flows of polymer solutions in abrupt contractions using an arbitrary Lagrangian Eulerian (ALE) based finite element method," *J. Non-Newton. Fluid Mech.*, 143(2-3), pp. 157-169.

[74]ANSYS® Academic Research, "Release 16.2."

[75]Anwar, M. R., Camarda, K. V., and Kieweg, S. L., 2015, "Mathematical model of microbicidal flow dynamics and optimization of rheological properties for intra-vaginal drug delivery: Role of tissue mechanics and fluid rheology," *J. Biomech.*, 48(9), pp. 1625-1630.

[76]Dealy, J. M., 2010, "Weissenberg and Deborah numbers - their definition and use," *Rheology Bulletin*, 79, pp. 14-18.

[77]Whitmore, T., 2016, "Computational molecular design of cellulose-based delivery vehicle for vaginal microbicide gels," Dissertation, University of Kansas.

[78]Egorov, V., van Raalte, H., and Lucente, V., 2012, "Quantifying vaginal tissue elasticity under normal and prolapse conditions by tactile imaging," *Int. Urogynecol. J.*, 23(4), pp. 459-466.

[79]Eskandari, H., Salcudean, S. E., Rohling, R., and Ohayon, J., 2008, "Viscoelastic characterization of soft tissue from dynamic finite element models," *Phys. Med. Biol.*, 53(22), pp. 6569-6590.

[80]Pacey, M., 2016, "The development and characterization of a novel instrument for measuring vaginal closing force: EVE the elevated-surface vaginal elastometer," Dissertation, University of Kansas.